Institute of Physics
Polish Academy of Sciences



Recognition of the Parameters of Colloidal Suspensions using Convolutional Neural Networks: from Bulk to Microdroplets

By

Kwasi Nyandey

Thesis submitted to the Institute of Physics, Polish Academy of Sciences, Warsaw, Poland, in partial fulfilment of the requirements for the award of Doctor of Philosophy Degree in Physics

June 2025

Declaration

Candidate's Declaration

I hereby declare that this thesis is the result of my own original research and that no part of it has been presented for another degree in this university or elsewhere.

Candidate's Signature…… Date 13.06.2025
Name: Kwasi Nyandey

Supervisor's Declaration

As written in my opinion to the Scientific Council of the Institute of Physics, Polish Academy of Sciences, the doctoral dissertation meets the requirements set out in Article 187 of the Act of 20 July 2018 Law on Higher Education and Science.

Supervisor's Signature Daniel Jakubczyk Date 13.06.2025
Name: dr. hab. eng. Daniel Jakubczyk, prof. IFPAN

Abstract

This Ph.D. Thesis is part of a larger project aimed at developing an optical-numerical system for the rapid identification of suspensions in microdroplets. Two elastic light scattering phenomena were employed and combined with machine learning to carry out three separate experimental studies, focused primarily on characterising the properties of suspensions. The two scattering phenomena were: (i) scattering of light by individual spherical microdroplets, generating interference fringes, which allowed for the direct application of Lorenz-Mie theory; and (ii) scattering by an ensemble of particles undergoing Brownian motion in a liquid medium, where time-dependent random interference patterns enabled the use of speckle method/theory.

In applying the Lorenz-Mie theory and its corresponding experimental method, microdroplets were produced from pure liquids, liquid–liquid mixtures, and suspensions, and were levitated in an electrodynamic trap to measure their light scattering patterns during evaporation. A carefully designed optical system, which enabled observation at angles close to 90°, allowed for the acquisition of well-resolved scattering patterns from all types of microdroplets.
To train a convolutional neural network for classification tasks, a set of theoretical light scattering patterns was generated over a broad droplet radius range (1–30 μm). These patterns were grouped into multiple classes defined by narrow radius intervals (initially 30 nm). The trained network was then used to classify experimentally recorded scattering patterns from evaporating droplets, thereby tracking the temporal evolution of their radii.
It was shown that, in the second iteration, reducing the class interval from 30 nm to 10 nm significantly improved classification accuracy, and the error in radius estimation could be reduced to as low as ±5 nm. Overall, classification accuracy was very high for microdroplets composed of pure liquids. In contrast, for microdroplets of liquid mixtures and suspensions, performance was affected by variations in refractive index and by distortions of internal optical fields caused by suspended nanoparticles, among other factors.
In the application of the speckle method, dynamic speckle patterns were measured for two sample types: (i) milk – a complex colloidal suspension – contained in a thin cuvette with a thickness of 50 μm (referred to as the "bulk medium"), and (ii) individual microdroplets of controlled monodisperse suspensions (referred to as the "microdroplet medium").
In the bulk medium, a 1.7 mm laser beam was used to generate transmission speckles, which were recorded at a near-forward angle of 26.9°, using four different exposure-time protocols. Following standard procedure, the recorded data was divided into "Training," "Validation," and "Test" sets for training the neural network. Additional "Independent" data sets were acquired separately and used to evaluate the stability and generalisation capability of the trained networks. All exposure-time protocols yielded very high classification accuracies on the "Test" sets; however, training robustness and generalisation performance on the "Independent" sets varied across protocols. Among them, one methodologically sound protocol was identified as optimal.
The third experimental study focused on the microdroplet medium, where a single microdroplet was treated as a microscopic cuvette containing a small number of nanoparticles. Multiple droplets were generated from suspensions with varying concentrations, as well as

from samples of fixed concentration but differing droplet sizes. These droplets were levitated in a different electrodynamic trap and observed using a separate optical system. Nevertheless, as in previous experiments, random interference patterns (speckles) produced by nanoparticles were recorded at angles near 90°. The convolutional neural network was trained following a similar approach as before. While the classification accuracy on the “Test” sets remained very high, the limited dataset size meant that this experiment was considered a proof of principle, offering valuable recommendations for further investigation.

Streszczenie (in Polish)

Niniejsza rozprawa doktorska jest częścią większego projektu, którego celem jest opracowanie optyczno-numerycznego systemu do szybkiej identyfikacji zawiesin w mikrokroplach. W pracy wykorzystano dwa zjawiska elastycznego rozpraszania światła, które połączono z metodami uczenia maszynowego, aby przeprowadzić trzy odrębne badania eksperymentalne, koncentrujące się głównie na charakteryzowaniu właściwości zawiesin. Zjawiska, o których mowa to: (i) rozpraszanie światła przez pojedyncze kuliste mikrokrople – tworzące prążki interferencyjne i umożliwiające bezpośrednie zastosowanie teorii Lorenza-Mie'go, oraz (ii) rozpraszanie przez zespół cząstek podlegających ruchom Browna w ciekłym ośrodku – tworzące zmienne w czasie, losowe obrazy interferencyjne – wzory plamkowe, pozwalające na zastosowanie metody/teorii „speklowej".

W metodzie eksperymentalnej wykorzystującej teorię Lorenza-Mie'go, wytwarzano mikrokrople z czystych cieczy, mieszanin ciecz–ciecz oraz zawiesin, lewitowano je w pułapce elektrodynamicznej i rejestrowano obrazy rozproszeniowe podczas ich parowania. Starannie zaprojektowany układ optyczny, umożliwiający obserwację pod kątem zbliżonym do 90°, pozwalał na rejestrację widocznych prążków interferencyjnych dla wszystkich typów mikrokropel.

W celu wytrenowania konwolucyjnej sieci neuronowej do zadań klasyfikacyjnych, wygenerowano zestaw teoretycznych obrazów rozproszeniowych – prążków interferencyjnych dla szerokiego zakresu promieni kropli (1–30 μm). Obrazy te pogrupowano w wiele klas o wąskich przedziałach promieni (początkowo 30 nm). Wytrenowana sieć była następnie użyta do klasyfikacji eksperymentalnie zarejestrowanych obrazów rozproszeniowych od parujących mikrokropel, co pozwalało na śledzenie czasowej ewolucji ich promienia.

Wykazano, że w drugiej iteracji zmniejszenie przedziału promieni z 30 nm do 10 nm istotnie zwiększyło dokładność klasyfikacji, a błąd oszacowania promienia mógł zostać zredukowany nawet do ±5 nm. Zasadniczo, dokładność klasyfikacji była bardzo wysoka dla mikrokropel z czystych cieczy. Natomiast w przypadku mikrokropel z mieszanin cieczy oraz zawiesin, skuteczność klasyfikacji była ograniczana przez zmienność efektywnego współczynnika załamania światła oraz deformacje wewnętrznych pól optycznych mikrokropli, spowodowane obecnością zawieszonych nanocząstek (a także inne czynniki).

W metodzie wykorzystującej teorię „speklową", dynamiczne obrazy interferencyjne – wzory plamkowe, rejestrowano dla dwóch typów próbek: (i) mleka – złożonej zawiesiny koloidalnej – umieszczonego w cienkiej kuwecie o grubości 50 μm („ośrodek objętościowy") oraz (ii) pojedynczych mikrokropel kontrolowanych zawiesin monodyspersyjnych („ośrodek mikrokroplowy").

W przypadku ośrodka objętościowego, transmisyjne wzory plamkowe (spekle) generowano za pomocą wiązki laserowej o średnicy 1,7 mm i rejestrowano pod kątem 26,9°, stosując cztery różne protokoły czasów ekspozycji. Zgodnie z powszechnie przyjętą procedurą, dane dzielono na zbiory „Uczący", „Walidacyjny" i „Testowy" do trenowania sieci neuronowej, natomiast dodatkowe niezależne zbiory danych („Niezależne") pozyskiwano osobno w celu oceny stabilności i zdolności uogólniania wytrenowanych sieci. Wszystkie protokoły ekspozycji dawały bardzo wysokie dokładności klasyfikacji na zbiorach „Testowych"; jednak

stabilność treningu oraz zdolność uogólniania wyników na zbiorach „Niezależnych” różniły się w zależności od protokołu. Spośród nich wyłoniono jeden, metodologicznie najlepiej uzasadniony wariant.

Trzecie badanie eksperymentalne dotyczyło ośrodka mikrokroplowego, gdzie pojedyncza mikrokropla była traktowana jako mikroskopijna kuweta zawierająca niewielką liczbę nanocząstek. Wytworzono wiele kropli z zawiesin o różnych koncentracjach nanocząstek, a także z tej samej zawiesiny, lecz o różnych rozmiarach kropli. Krople te były lewitowane w innej pułapce elektrodynamicznej i obserwowane za pomocą odmiennego układu optycznego. Podobnie jednak jak w poprzednich eksperymentach, wzory plamkowe generowane przez nanocząstki były rejestrowane dla kątów zbliżonych do 90°. Konwolucyjną sieć neuronową trenowano zgodnie z wcześniej zastosowaną procedurą. Choć dokładność klasyfikacji na zbiorach „Testowych” pozostała bardzo wysoka, ograniczona liczba danych sprawiła, że badanie to pokazało tylko możliwości metody i posłużyło do sformułowania zaleceń na potrzeby przyszłych prac badawczych.

Acknowledgements

First and foremost, I thank The God and Father of our Lord Jesus Christ, because His grace was sufficient in my weakness.

My heartfelt gratitude goes to my supervisor, dr. hab. eng. Daniel Jakubczyk, Prof. IFPAN, for his dedicated support which he started even before my acceptance to the Ph.D. School. His unwavering love as a mentor was not bound to only academics but stretched out to social and even religious environment, which I feel incredibly fortunate to have experienced during the few years of my Ph.D. programme.

I am equally thankful to Dr. Gennadiy Derkachov for his immense support during my experimentations and all the extensive discussions we have had about each topic that we laid our hands (or "minds") on. It was a blessing and an enlightenment working and speaking with him.

I also express my sincere gratitude to Prof. Yarosław Shopa for the collaboration and the various experiments we conducted together. His dedication was a motivation in itself and I was privileged to work under him.

Dear Pan Sławomir Palesa, our most able and hardworking Technician, your handiworks can be seen everywhere in the laboratory so I am quick to say that I accomplished tasks because of you. Thank you Pan Sławomir Palesa.

I am equally thankful to the rest of the group members, Prof dr. hab. Maciej Kolwas for your regular enquiry about my progress, Prof. dr. hab. Krystyna Kolwas, and Dr. Anastasiya Derkachova for the constructive questions and guidance during my studies and most importantly during all my presentations and our co-authored publications.

I am forever indebted to my wife, Theresa, for being patient in my absence and single handedly taking care of our children while I was pursuing my Ph.D. programme. For my family and fellow Christians in International Christian fellowship in Poland and University Interdenominational Church in Ghana, thank you for your prayers.

Finally, I appreciate and acknowledge NAWA, Poland for sponsoring my one-month research visit to Germany and National Science Centre, Poland for financially supporting my Ph.D. programme under the grant: 2021/41/B/ST3/00069

List of symbols

a_d – Radius of microdroplet

m_d – Refractive index of the microdroplet

m_s – Refractive index of the microdroplet's surrounding medium

m_r – Relative refractive index

x_d – The microdroplet's size parameter

k_s – Wave number in surrounding medium (free space)

k_d – Wave number in the droplet medium

$\vec{E}$ – Time-harmonic electric field component of the plane electromagnetic wave

E_o – Electric field amplitude.

$\vec{H}$ – Time-harmonic magnetic field component of the plane electromagnetic wave

ω – Angular frequency

ε – Electric permittivity constant

μ – Magnetic permeability constant

$\vec{M}$ & $\vec{N}$ – Vector harmonic functions

ψ – A scalar function or generating function for the vector harmonic functions

$\vec{C}$ – A constant or guiding vector

$\vec{r}$ – Radius vector or distance vector

θ – Azimuth angle measured from the incident beam propagating along the x-axis

ϕ – Zenith angle measured from the z-axis

m and n – Separation constants

$z_n(k_s r)$ – Any of the four spherical Bessel functions $j_n(\rho)$, $y_n(\rho)$, $h_n^{(1)}(\rho)$, $h_n^{(2)}(\rho)$

a_n and b_n – The scattering coefficients of the scattered wave

$S(\theta,\phi)$ – Scattering matrix

I_V and I_H – Vertical and horizontal components of intensity functions of polarized scattered light.

φ_{uvw} – Random phase angle associated with a scatterer

c – Speed of light

r_{uvw} – Distance between scatterer and observation point

$\vec{q}_{wv}$ – Scattering wave vector

$\vec{k}_{sc}$, $\vec{k}_{in}$ – Wave or momentum vectors for scattered and incident wave

α, β, γ – Coefficients

e – Charge of a particle (microdroplet)

U – DC voltage

V – Amplitude of AC voltage

List of acronyms

LMT	– Lorenz-Mie theory
GLMT	– Generalized Lorenz-Mie theory
T-matrix	– Transition matrix
FDTD	– Finite-difference time domain
MMP	– Multiple multipole
CCD	– Charged couple device
MODE	– Millikan oil drop experiment
PMT	– Photomultiplier tube
RBF	– Radial basis function
MLP	– Multilayer perceptron
CNN	– Convolutional neural network
SEM	– Scanning electron microscopy
ReLU	– Rectified linear unit
AC	– Alternating current
DC	– Direct current
PID	– Proportional integral derivative
DEG	– Diethylene glycol
DPG	– Dipropylene glycol
PS	– Polystyrene
ADAM	– Adaptive moment estimation
SGDM	– Stochastic gradient descent with momentum

Table of contents

Declaration ii
Abstract iii
Streszczenie (in Polish) v
Acknowledgements vii
List of symbols viii
List of acronyms ix
Table of contents x
List of publications and participation in conferences xii

CHAPTER 1 1

Introduction 1
1.1 Chapter overview 1
1.2 The Mie theory and its extensions 1
1.3 Other light scattering theories 2
1.4 Multiple particles scattering 4
1.5 Laser speckles 5
1.6 Experimental techniques in optical particle characterization 6
1.7 Neural networks and their applications in light scattering 7
1.8 Statement of the problem 9

CHAPTER 2 10

Theoretical Background 10
2.1 Chapter overview 10
2.2 The Lorenz-Mie theory: scattering by spherical particles 10
2.2.1 Solutions to the vector wave equations using vector spherical harmonics 10
2.2.2 Expanding the incident plane wave and the scattered fields in vector spherical harmonics 12
2.2.3 Scattering matrix and the scattered intensities 13
2.3 The speckle phenomenon 15
2.3.1 Light scattering by microdroplets of colloidal suspension ("microdroplet medium") 17
2.4 Convolutional neural networks: theoretical background 18
2.4.1 The final activation and error functions 19
2.4.2 Convolutional neural network architecture 20
2.5 Electrodynamic particle levitation 21

CHAPTER 3 25

Experimental Methods 25
3.1 Chapter overview 25
3.2 Recognition of concentration-driven speckle changes from the "*bulk medium*" of a real-world suspension (milk) 25
3.3 Droplet sizing and tracking of evaporating microdroplets of pure liquids, liquid mixtures and suspensions . 26
3.3.1 The trap, levitation of droplets and evaporation 26
3.3.2 Droplet injector design and injection 27
3.3.3 Sample preparation 28
3.3.4 Experimental considerations and measurement of Mie scattering patterns 28
3.4 Parameter-driven speckle changes from microdroplets of suspensions 30
3.4.1 Concentration-driven speckle changes 31
3.4.2 Size-driven speckle changes 32

CHAPTER 4 33

Results and Discussions 33

4.1 CHAPTER OVERVIEW 33
Part I 33
4.2 INVESTIGATION OF PARAMETERS OF SUSPENSIONS IN THE *"BULK MEDIUM"* 33
4.2.1 Supplementary materials in online data repository 33
4.2.2 Summary of publication 33
4.2.3 A copy of the published article 33
Part II 34
4.3 CLASSIFICATION OF RADIUS EVOLUTION AND TRACKING THE EVAPORATION RATE OF MICRODROPLETS OF PURE LIQUIDS AND SUSPENSIONS 34
4.3.1 Supplementary materials in online data repository 34
4.3.2 Summary of publication 34
4.3.3 A copy of the published article 34
4.3.4 Supplementary results (unpublished) 35
(i) Supplementary results for pure DEG 35
(ii) Supplementary results for DEG + PS 36
(iii) Supplementary results for DPG + H_2O 37
(iv) Supplementary results for DPG + H_2O + SiO_2 38
Part III 39
4.4 CLASSIFICATION OF SIZE- AND CONCENTRATION-DRIVEN SPECKLE CHANGES RECORDED FROM THE "*MICRODROPLET MEDIUM*" 39
4.4.1 Size-driven speckle changes from the "microdroplet medium" 39
4.4.2 Concentration-driven speckle changes from the "microdroplet medium" 40
4.5 COMPARISON BETWEEN THE "BULK MEDIUM" AND "MICRODROPLET MEDIUM" 43
CHAPTER 5 44
Summary, Conclusions and Recommendations 44
5.1 CHAPTER OVERVIEW 44
5.2 SUMMARY AND CONCLUSIONS 44
5.3 RECOMMENDATIONS 45
5.4 APPENDIX 46
5.5 REFERENCES 48

List of publications and participation in conferences

Publications resulting from the Ph.D. studies included in the Thesis:

- **K. Nyandey** and D. Jakubczyk, "*Combining transmission speckle photography and convolutional neural network for determination of fat content in cow milk: an exercise in classification of parameters of a complex suspension*," Eur. Phys. J. Plus, vol. 139, no. 2, Feb. 2024.
- **K. Nyandey**, G. Derkachov, and D. Jakubczyk, "A convolutional neural network technique for online tracking of the radius evolution of levitating evaporating microdroplets of pure liquids, liquid mixtures and suspensions," *J. Quant. Spectrosc. Radiat. Transf.*, vol. 344, no. 2024, p. 109533, May 2025.

Other publications during Ph.D. studies

- Y. Shopa, M. Kolwas, I. Kamińska, G. Derkachov, **K. Nyandey**, T. Jakubczyk, T. Wojciechowski, A. Derkachova, and D. Jakubczyk. "*Luminescent nanoparticles in a shrinking spherical cavity–probing the evaporating microdroplets of colloidal suspension–optical lattices and structural transitions*." Journal of Quantitative Spectroscopy and Radiative Transfer 296, 108439, Feb. 2023.
- D. Jakubczyk, G. Derkachov, **K. Nyandey**, S. Alikhanzadeh-Arani, and A. Derkachova. *"Chromatic dispersion and thermal coefficients of hygroscopic liquids: 5 glycols and glycerol."* Scientific Data 10, no. 1, 894, Dec. 2023.
- D. Jakubczyk, G. Derkachov, **K. Nyandey**, S. Alikhanzadeh-Arani, and A. Derkachova. *"Author Correction: Chromatic dispersion and thermal coefficients of hygroscopic liquids: 5 glycols and glycerol."* Scientific Data 11, no. 1, 727, Jul. 2024.
- P. Osei-Wusu Adueming, J. Opoku-Ansah, A. Atiogbe Huzortey, C. Lloyd Yeboah Amuah, **K. Nyandey**, M. Jojo Eghan, B. Anderson, and S. Sonko Sackey. *"A Feasibility Study on Monitoring Shelf Life of Bottled Natural Fruit Juice Using Laser-Induced Autofluorescence."* International Journal of Optics 2023, no. 1, 7458190, Apr 2023.

Publications before Ph.D. studies

- T. OS Akowuah, E. Teye, J. Hagan, and **K. Nyandey.** *"Rapid and nondestructive determination of egg freshness category and marked date of lay using spectral fingerprint."* Journal of Spectroscopy 2020, no. 1, 8838542, Oct. 2020.
- C. LY Amuah, E. Teye, F. P. Lamptey, **K. Nyandey**, J. Opoku-Ansah, and P. Osei-Wusu Adueming. *"Feasibility study of the use of handheld NIR spectrometer for simultaneous authentication and quantification of quality parameters in intact pineapple fruits."* Journal of Spectroscopy 2019, no. 1, 5975461, Aug. 2019.

Conferences presentations, summer school and research visit during Ph.D. studies

- **Oral presentation:** "*Classification of milk fat content categories based on speckle pattern using machine learning"*, 13th International conference series on Laser-light and interactions with particles. Optical particle characterization follow-up, 21 – 26th August, 2022, IFPAN. (funding: Travel grant, European Physical Society)

- **Oral presentation:** *"Convolutional neural network can track the radius evolution of levitating-evaporating microdroplets"*, 14th International conference series on Laser-light and interactions with particles. Optical particle characterization follow-up, 18 – 22nd September, 2024, School of Physics, Xidian University, Xi'an, China. (funding: National Science Centre, Poland, grant 2021/41/B/ST3/00069)

- **Summer school**, Topic: *Charged particle traps,* Institute of Physics, Nicolaus Copernicus University, Torun, Poland, 10 – 12th July, 2023. (funding: National Science Centre, Poland, grant 2021/41/B/ST3/00069)

- **Research visit,** Topic: Light scattering-based measurements of small particles and biological cells in suspension, using 1) scattered-light imaging of single particles in flow cytometry and 2) collimated transmittance spectroscopy for particle ensembles. Physikalisch-Technische Bundesanstalt (PTB), Department of Biomedical Optics, Berlin, Germany, 2nd February – 2nd March, 2024, (funding: NAWA).

Oral presentations in Ph.D. student symposia

- **Oral presentation:** "*Classification of milk fat content categories based on speckle pattern using machine learning"*, 20th September, 2022, Zoom platform

- **Oral presentation:** "*Tracking the evolution of radius of levitated shrinking micro-droplet: an exercise in deep learning*", 7th June, 2023, Zegrze, Poland

- **Oral presentation:** "*Convolutional Neural Networks can track the radius evolution of levitating-evaporating microdroplets*", 4th June, 2024, Zegrze, Poland

Chapter 1
Introduction

1.1 Chapter overview

The general subject of light scattering is a multifaceted field of disciplines. Hence, a complete review would probably involve several volumes, which in some sense already exists. Consequently, in this chapter, we will focus on briefly reviewing the Mie theory, its extensions and other light scattering theories, providing comparisons when relevant. Since these scattering theories are generally restricted to single particle scattering, other attempts to solve the problem of scattering involving multiple particles will be explored. A brief review of speckle which is concerned with the random intensity distribution recorded from scattering by an ensemble of particles (both static and dynamic) is also presented. Afterwards the experimental techniques pertaining to scattering by single particles and a system of multiple particles will be reviewed. Finally, a brief review of neural networks and their applications specific to light scattering data processing will also be presented. For each of these brief reviews presented here, original works as well as the great and comprehensive reviews in literature will be cited for the interested reader. The chapter will be concluded with the statement of the problem.

1.2 The Mie theory and its extensions

N. A. Logan [1] published a survey of the early contributors to the field of elastic scattering of plane electromagnetic waves by a sphere in which he named Ludwig Lorenz (1829 – 91), Alfred Clebsch (1833 – 72), Lord Rayleigh (1842 – 1919), James Clerk Maxwell (1831 – 79) and Gustav Mie (1868 – 1957) among other equally important contributors. Hence, it is needless to emphasize that this field has been investigated as far back as the nineteenth century. As noted by G. Gouesbet [2], (with a recommendation to write "Lorenz-Mie theory" instead) the year 2008 marked a century of Gustav Mie's publication with series of commemorations in the scientific community and across institutions, indicating the long-standing fame of the theory. It is perhaps, the widely applied theory, though, known originally to be restricted to plane wave scattering by a homogeneous, isotropic and non-magnetic sphere in a non-absorbing medium.

The Lorenz-Mie theory (LMT), in summary, involves expressing the wave equation in spherical polar coordinates and separation of variables to obtain the Mie scattering coefficients from the analytical solutions [3]. In other words, the incident, internal and outgoing/scattered waves are expanded into vector spherical harmonics [4]. Then, by applying the appropriate boundary conditions, the scattered field can be expressed and the coefficients determined by matching the components between the internal and scattered field. The field, which is a superposition of the electromagnetic normal modes with each multiplied by the appropriate coefficients [4]) may then be sketched out as done by Mie in his original paper [5] and also [4]. The most relevant aspect of this endeavour, to this study, is the visualization/imaging of the fields (in terms of scattered intensities) with the general purpose of relating the optical properties and scattering characteristics to a sphere of given size. This approach is commonly

used in particle characterization, a subject matter that is well established in literature [6][7]. The original publication by Gustav Mie (in German) [5], its first English translation [8] and subsequent treatments in textbooks and reviews [4][9][10][11] are available for the interested reader. There is also a dedicated light scattering information portal [12] with a special section for Mie theory and its 100 years celebration [13].

There are, however, modern extensions of the LMT beyond some of its original restrictions to cover anisotropic [14] and coated spheres [15]. While others explored the small-particles and their parameter limits of the LMT [16]. Other theories (details in the next section) have also been developed which circumvents other restrictions of the LMT such as magnetic spheres [17], single- and multiple-coated dielectric [18], and several other particles (see the review by [3]). The incident wave has also been modified to include arbitrary shaped beams [2][19] – a discipline which has been carefully and well developed to maturity with experimental confirmations by Gouesbet and co-workers [2] as well as other researchers [20]. It is popularly known as Generalized Lorenz-Mie Theory (GLMT). The beam, which must be a transversely focused and a solution to the Maxwell's equations, is then expanded into basis functions (infinite series of spherical Bessel functions and spherical harmonics [19] [2]) with each multiplied by a coefficient describing the beam shape, hence the name "beam shape coefficients" [21]. The scattering particles, on the other hand, must possess a high degree of symmetry in which case the Maxwell's equations can be solved, using the method of separation of variables [21] as in the case of LMT. It must however, be emphasized that GLMT has also been extended to cover other kinds of scattering particles such as spheroids, cylinders and stratified spheres (see the review [21]). Other methods of expanding the beam have been reported [19], as well as different methods of evaluating the beam shape coefficients [2].

Undoubtedly, the availability of computer codes for a scattering theory plays an enormous role in simulating and understanding related phenomena as well as designing laboratory and field optical techniques and systems [22]. Today, the LMT programmes are available in programming languages such as Fortran [4], C ++, Pascal, Java [23] and other platforms such as Mathematica, Maple and MATLAB. In 2008, T. Wriedt demonstrated (with some numerical errors in labelling the axis) the possibility of porting LMT software on a mobile phone through Java runtime environment using MATLAB clone [24]. Another interesting usage of the LMT is its comparison with more complex scattering theories to validate their applicability (see e.g. [25][26][27]).

1.3 Other light scattering theories

In the same sense of developing more complex theories capable of solving the scattering of light by shape-, material- and size-specific particles, the transition matrix (T-matrix) [28][29][30][31] or extended boundary condition method, the point matching, the method of moments, generalized multipole technique, the transmission line matrix, finite element, finite-difference time domain, discrete-dipole approximation, which have all been treated extensively in the textbooks Mishchenko et al., [32][33]. It is also worth mentioning that earlier, the Rayleigh theory [4] and the geometric optics approximations [34] existed, respectively, for particles with sizes much smaller than and much larger than the wavelength. The gap between this size region (the so-called resonant region) appears to be filled by the above-

mentioned theories which basically explore different approaches to solve the scattering problem.

The transition matrix method (known in the original paper as matrix formulation [35] and with further emphasis from G. Gouesbet [30], to be called a formulation instead of a method), was first proposed by P. C. Waterman. He proposed the formulation for computing the scattering of electromagnetic wave by a smooth, perfectly conducting arbitrary nonspherical particle. The scattered fields are represented by electric dipoles whose response are proportional to the induced surface current at points over the entire surface of the scatterer. Then by application of the boundary condition that the scattered field cancels the incident fields, the surface current can be determined. Interested readers may also find more about the formulation for nonspherical particles in the review by [31] and in the textbook [32]. Nonetheless, G. Gouesbet [30] has jointly explored this formulation and the GLMT for spherical particles. Where he outlined the differences between the two, in terms of their standard approach to obtaining expansion coefficients of the scattered fields. The T-matrix relies on the expansion of only the incident and scattered electromagnetic fields to relate their coefficients through a transition matrix. Whereas GLMT applies an arbitrary shaped electromagnetic beam to a regular particle, in which case the Maxwell's equations can be solved by separation of variables, as stated earlier. However, by using vector spherical wave functions in GLMT, the T-matrix formulation for GLMT was found [30]. Though its applicability in experimental configurations has not been demonstrated yet (to the best of my knowledge), the approach seems to be a very interesting finding.

The Point Matching Method (as in LMT) uses a plane wave illumination and expands the scattered and internal fields in terms of spherical vector wave functions which satisfy Maxwell's equations. However, (unlike the LMT) point matching and least-squares fitting is applied to satisfy the boundary conditions on the surface of the sphere. It has been applied for the computation of scattering by raindrops [36] – (very) large droplets are difficult to handle with GLMT or T-matrix formulation. Interested readers are referred to the review by T. Wriedt [3], specifically to the subsection "*Point Matching Method*" where there is a detailed review and a comparison between this method, the T-matrix formulation and the LMT, outlining both similarities and differences with extensive citations.

Finite-difference time domain (FDTD) method was originally designed to apply numerical methods to compute the scattering of electromagnetic waves by non-spherical and inhomogeneous particles [33][37]. However, apart from rectangular particles, it has been shown afterwards not to pose such strict treatment to geometry and homogeneity [27][38]. Hence, some authors have found good agreements between its results and the LMT for the scattering of electromagnetic waves by small ice spheres and hexagonal ice crystals [27]. The method (and its discretization algorithm) was first proposed by K. S. Yee [39]. It generally involves expressing the Maxwell's equations in Cartesian coordinate system to obtain the set of scalar partial differential equations. A corresponding set of finite difference equations are then formulated by assuming a perfect conductor with vanishing normal components of the magnetic and tangential components of the electric fields at the surface. This then allows for the discretization of the scattering particle's volume and parts of its surrounding into subwavelength

grid-size cells [37]. The approach is, in other words, described as discretization of the Maxwell's equations using finite-difference in space and time [27]. This enables the near-field at each grid point to be evaluated in time-matching iterations until a steady-state solution is obtained [3]. Despite the good agreements obtained between Finite-difference time domain method and the LMT, a few error sources (e.g. grid size, staircasing-effect and truncation effect) as well as computational bottlenecks and its disadvantageous computer resource requirements have been identified and discussed extensively by several authors [3][27]. Other methods employing similar discretization are the finite element method [37], and transmission line matrix method [3].

The generalized multipole technique (known also as the multiple multipole method/model (MMP) see details in [40]) is yet another scattering theory in which one can find both similarities and differences with LMT. The technique, when applied to a sphere, employs multipole expansion in the sense that it uses a set of discrete spherical waves (which are solutions to the Maxwell's equations) as sources. However, unlike the LMT in which the origin of a single source coincides with the origin of the sphere, multiple origins (displaced from the surface where the boundary conditions are applied [40]) are employed. Furthermore, while the LMT applies the orthogonality and completeness of wave functions to evaluate the fields, the generalized multipole technique uses basis functions whose unknown coefficients are to be determined by either point matching [40], surface integral or least-square error estimation [3], after applying the appropriate boundary conditions. Analogous to the LMT, some authors have evaluated the current and surface fields analytically from the discrete spherical wave equations [40].

1.4 Multiple particles scattering

Though the above light scattering theories and the many others (not reviewed in this study) generally deal with single particles, the problem is much complex in a system of multiple particles. The simplest model in this case is that of scattering by two spheres as demonstrated by Bruning and Lo [41] (and the references therein) comparing multipole expansion and ray optics solutions. In their analysis, they considered several approximations, the three most relevant to this study are: (i) the axial symmetric and broadside illumination of two identical spheres, with distances of separation equal to or far greater than the radius of one, (ii) one sphere is in the other's shadow with end-fire illumination and (iii) a system in which the spheres are in contact. These approximations are particularly interesting since they lead to the solutions of scattering scenarios which are often encountered in evaporating microdroplets of colloidal suspensions. Thus, the suspended particles may be initially separated but tend to approach each other as the droplet evaporates [42]. Modern reports in the literature about the same subject matter, specifically for multiple scattering regime can be found in the review by T. Wriedt [3]. G. Gouesbet and G. Grehan [43] applied GLMT to solve the scattering by a system in which a single spherical inclusion is embedded at an arbitrary location inside a larger sphere. The authors provided a list of its possible practical applications in particle characterization using phase-Doppler instruments and rainbow refractometry as well as the possibility to extend the theory to a sphere embedded with many inclusions, another typical analogue of droplets of suspensions.

1.5 Laser speckles

Beside these complex theories, there is yet another parallel branch of electromagnetic scattering treatment which is concerned with investigating the random intensities produced by an ensemble of many but small particles without the need for the rigorous theoretical treatment of individual particles as in the theories above. It is widely known as laser speckles, which is the random 3D interference patterns formed when a coherent radiation (a laser beam) is reflected from an optically rough surface or transmitted through a translucent material [44][45][46]. The randomness result from the random positions of the scatterers and refractive index variations [44]. Because of this randomness of the intensities, probability theory and statistics analysis have been used to described its properties, even as far back as the nineteenth century using fairly coherent light. Dainty in his book published in 1975 [44], listed six main areas in which speckle pattern was applied after the invention of the laser. Two of these areas most relevant to this study are (i) *fundamental statistical properties of laser speckles* and (ii) *measurement of surface roughness*. Hence, in chapter 2 review of relevant literature to these areas will be presented and refer interested readers to the detailed treatments in his book and other literatures [47][48].

Nonetheless, it is worth stating that in the statistical treatments of laser speckles, "*a random walk in the complex plane*" model is often adopted [44][47][48] – an earlier classical concept employed in analysis of random vibrations [49][50]. Speckle patterns are either considered as isolated scattering areas [44] or as a continuum [47]. The former approach usually starts from the contribution of a single scatterer to the interference at a point on the observation screen or detector (e.g. single CCD pixels). The resultant amplitude and hence intensity and phase at the chosen point is then obtained by a summation or integration over many scatterer contributions. This approach was used by Goodman to derive the first-order statistics of the complex amplitude, intensity and phase of laser speckle patterns [44]. Lord Rayleigh, in a much earlier publication, used a similar approach to find the resultant and hence probability of a very large number (n) of vibrations of equal amplitude and arbitrary phases [49]. While choosing a single CCD point is the widely accepted approach for analysing speckles, it must be noted that, practically, the individual bright speckles in the pattern usually cover elemental regions which are significantly larger than a CCD pixel or the chosen point. Hence it is best described as a multi-lobed intensity pattern [51]. These lobes are not only located at random positions but are also characterized by different lengths and widths, irregular edges, and many unequal amplitudes.

Furthermore, by exploring the likelihood of finding a bright point of high or a dark point of zero intensity [49], the probability density function (from the first-order statistics [44]), the autocorrelation function and power spectral density (from the second-order statistics [51] have been obtained. It must be noted, however, that the above-mentioned analysis, though, may be applied on both reflection and transmission speckles from static scatterers, the patterns vary only spatially but not temporally. This property, of course, has been exploited extensively in characterization of material surfaces and smoothness investigations (using speckle imaging/photography) [46][52], measurement of material strength and small displacements

(using interferometric setups, sometimes combined with cantilever systems [53]), to mention a few.

Upon the inclusion of dynamic systems (generally colloidal suspensions or dynamic biological systems) as samples of interest, either the spatial or temporal or both variations can be used for measurements. A resourceful textbook (by Nikita A. Fomin [54]) specific to the application of speckle photography in the field of fluid mechanics, provides both theoretical and experimental considerations of both static and dynamic speckles. A similar textbook [55] exists for the applications of speckles in Biology for the interested reader. It is reported that two fundamental speckle motions result in such dynamic samples – translational motion (when the whole pattern moves without change in shape within small displacement) and *boiling* of speckles (when there is no movement but rather individual deformations with a characteristic sense of disappearing and reappearing) [54]. As stated earlier, the most prominent analysis in this case is the analysis of space-time correlation functions.

1.6 Experimental techniques in optical particle characterization

In the field of optical particle characterization, optical methods combined with the possibility to isolate single particles or droplets have proven to be the preferred choice due to their accuracy, precision and sensitivity. As reviewed by [6][7] particle size and refractive index seem to be the dominating parameters of interest – among shape, particle counting, aggregation, diffusion, mobility, number density and velocity of particles in flow measurements. Also, by trapping particles, some existing light scattering theories have been verified experimentally. This subsection will be concerned with reviewing a few literatures related to trapping of single micro-particles/droplets and application of elastic light scattering for investigation.

E. James Davis [56] presented a detailed historical account, as well as scientific review of single aerosol levitation, which started with the first successful experimental separation of individual water droplets by Millikan [57] followed by the famous Millikan oil drop experiment (MODE) [58]. It has also been noted that (subsequently) several early researchers used the MODE to investigate the evaporation rate of droplets without the application of light scattering theories (see the review by E. James Davis [56]). Today, the subject matter of both trapping and generally, particle investigations have matured with consequential reports of different techniques of trapping and different disciplines and applications. Apart from electrodynamic trapping [59][60], there are optical [61][62] and acoustic [63] trapping techniques used as powerful tools in research and technology of microparticles. This is because, after successfully trapping single particle/droplet and regulating its movements to quasi-stationary position, accurate and precise characterization can be done.

Perhaps the first attempt to experimentally verify LMT was carried out by Gucker and Egan [64] who mounted a photomultiplier tube (PMT) on a rotatable stage to measure scattered intensity from a droplet as a function of angle, from the Millikan condenser. Their aerosol droplets were made from (low volatility) dioctyl phthalate and the measurements produced results of droplets diameters ranging from 0.7 to 1.5 μm. Their experimental results were compared with the theoretical Mie scattering patterns and sources of errors (from non-sphericity of droplets due to strong trapping electric fields, refractive index variation and ac-

curacy of the PMT among others) were determined and discussed. Modifications of their experiments by other researchers, in terms of automation, development of the setup into a commercial device (Differential II instrument [65]) and its subsequent usage in extensive research have been reviewed by E. James Davis [56]. The Differential II instrument in its first report in literature was demonstrated to levitate a 550 nm droplet whose diameter reduced to 495 nm within a period of 5 hrs, though the study was not aimed at measuring the evaporation of the studied liquids [65].

The study which was directly aimed at measuring the evaporation rates of submicron-aerosol droplets using a modified Differential II instrument was performed by E. James Davis and Edward Chorbajian [66]. Similar to the study by Gucker and Egan [64], they produced droplets from dioctyl phthalate. However, their experiment was performed at various pressures to investigate a list of theoretical analysis of evaporation of submicron-aerosol droplets. Furthermore, they used the LMT and validated the accuracy and sensitivity of their measurements using a polystyrene sphere of diameter 0.775 μm, comparing theory with experimental measurements and reporting a 1% variation. Earlier, attempts to study evaporation of droplets in terms of fundamental thermodynamics with and without application of light scattering have been cited by E. James Davis and Edward Chorbajian [66], and reviewed by E. James Davis [56].

A. K. Ray et al., [67] investigated (both theoretically and experimentally) the precision of elastic light scattering measurements involving three possible combinations of (constant and/or changing) size parameter and refractive index as well as a coated sphere with unknown outer radius and coating thickness. Other recent comprehensive reviews of elastic light scattering theories involving, mainly, single particle have been presented by [24] and [68]. The Group of Optical Characterization of Micro- and Nanoobjects, located in the Institute of Physics, Polish Academy of Sciences (in which I have been privileged to pursue my PhD), like several other research groups, have investigated the physics of microdroplets and nano-object for several decades.

1.7 Neural networks and their applications in light scattering

The methods or techniques employed in artificial neural networks (neural networks) are deeply rooted in diverse fields of study: mathematics, statistics, physics, engineering, computer science, all driven by neuroscience [69]. In recent years, the advancements of artificial intelligence and machine learning have led to the application of neural networks in pattern recognition [70], object classification/recognition and detection [71], modelling and signal/time-series processing and analysis [72], to mention a few. Though many applications such as image classification, object recognition and detections, involve illuminated objects, this section focuses on applications specific to the processing and analysis of light scattering patterns (from single or multiple particles) with the sole purpose of characterization and/or retrieval of the particle's optical properties. Among the many optical properties of particles or materials, shape, size (radius) and refractive index appear to be the most commonly sought-after parameters.

The reports of the used of neural networks in light scattering applications have been limited to a few types. Generally, a two-input (2-dimensional) network, with one hidden layer and

one output can be represented with a class of functions expressed as [73]: $y_k(\vec{X}) = \sum_{i=1}^{N} w_i f_i(\vec{X})$. Where f_i are some parametric (popularly known as activation) functions and w_i are coefficients, both to be estimated during network training and $\vec{X} = (X,Y)$ is vector of inputs. As can be inferred, the type of function (linear or non-linear) depends on the parametric functions f_i which then dictates the approximation scheme to be applied. Maruyama et al., [73] discussed into detail the two most common schemes – Regularization and Ridge function approximations. The Radial Basis Functions neural networks (RBF) apply regularization, defined as the weighted norm of the difference between the input vector and a centre vector (see [73] for details). In this case the parametric functions are fixed and the output function is linear in the coefficient parameter space. On the other hand, when the parametric functions are varied, non-linear output functions are obtained and ridge function approximation is applied. Among the many neural networks built for this purpose, those applying the perceptron (originally proposed by Frank Rosenblatt [[74]]) will be discussed here. The multilayer perceptron (MLP) type of neural network uses non-linear activation functions (sigmoid, hyperbolic tangent, etc). The rectified linear unit (ReLu, proposed by [75]) which performs thresholding operation to the input and *softmax activation* function [70], which enables Bayesian or probabilistic interpretation of the output, are both commonly used in convolutional neural networks (CNN) (see chapter 2 for details).

Ishimaru et al. [76] used the MLP type of neural network to retrieve particle-size distribution from backscattered light, remotely sensed from a volume containing spherical particles with radii distribution ranging from 0.01 to 40 μm. Since the main task of such an inverse problem is to accurately determine the size distribution, they trained the network using a log-normal size distribution function and reported percentage errors of < 10%. Ulanowski et al. [77], used Gaussian basis function in RBF neural network and generated theoretical light scattering vectors so that by a linear combination of the weighted basis function and a bias term, the network was trained. The output of the network then produced a two-column vector of predicted radii and refractive indices of the spherical scatterer. Though the study lacked experimental measurements to test the capabilities of the network and the proposed approach, the instability effect of truncating data from the near-forward (0 – 30^o) and near-backward (120 – 180^o) angles of the test data were simulated and the errors discussed. A similar study (as Ulanowski et al. [77]) was done by Vladimir V. Berdnik and Valery A. Loiko [78]. They used feed-forward neural network to retrieve the radius and refractive index from multi-angle light scattering data recorded from spherical particles in a flow cytometer setup. In application of light scattering and neural network to environmental monitoring, Kaye et al., [79] designed an optical instrument for measuring the characteristic laser scattering patterns of harmful airborne fibres. They used RBF neural network for classification. The technique is shown to produce very high classification accuracies of background and two classes of asbestos fibres (chrysotile and crocidolite).

1.8 Statement of the problem

This Thesis is part of a larger project, whose ultimate goal is to devise an optical-numerical method for recognition and classification of realistic suspensions in free microdroplets. The main concept is to utilize a deep neural network to classify speckle images that would be generated from such complex microdroplets. On the basis of the previous works (nanospheres suspension in thin cuvettes [80]) it was judged to be probably feasible. Hence, it was necessary to check whether real-world multi-parameter suspension in bulk could be recognized by using convolutional neural network to classify their speckle images, as the monodisperse nanoparticles were. Off-the-shelf UHT milk was chosen as the work-horse. The answer was positive [81], allowing the next step to commence.

However, the number of parameters that can be encoded in the interference/speckle patterns generated from microdroplets of suspensions is much more than those from the bulk of the same suspension in thin cuvettes. Firstly, the light scattering characteristics of the microdroplet as a spherical scatterer can be investigated. In which case, its parameters (size, refractive index and evaporation/condensation rate (if any)), as well as the parameters of the particles in its medium are encoded in its scattering patterns. Thus, CNN will be trained to recognize microdroplets of different sizes – naturally evaporating in an ambient atmosphere – using Mie scattering images/patterns.

Secondly, the microdroplet can serve as a micro-cuvette holding a small number of mono- or poly-dispersed nano-particles. In which case the parameters of the inclusions (size, refractive index, concentration) are encoded in the speckle patterns due to scattering as an ensemble of particles. Different speckle patterns can result from: (i) different concentrations of suspensions used to form the microdroplet (different initial concentration), (ii) different microdroplet sizes (the lager the droplet, the more scatterers). When the droplet evaporates, there is a mixture of the above: (iii) the droplet size decreases, but the total number of scatterers remains constant, and thus their concentration grows. In all of these cases, since the inclusions are constantly undergoing Brownian motion, the speckle patterns change dynamically while the changing parameter is encoded in the speckle recorded. The task here will be devoted to solving the first two (out of three) problems stated.

Detailed treatment of the relevant theoretical background for Mie theory, the speckle phenomenon, convolutional neural networks and electrodynamic trapping will be presented in chapter 2.

Chapter 2
Theoretical Background

2.1 Chapter overview

As mentioned in chapter 1, the theoretical background for: (i) Mie theory as presented by Bohren and Huffman [4] but geared towards the scattering of plane electromagnetic waves by transparent microdroplets in which Mie conditions apply, (ii) the speckle phenomenon for both scattering in a bulk and microdroplet media, (iii) convolutional neural networks and how it is applied to recognize light scattering patterns in classification tasks and (iv) finally, electrodynamic trapping and how it is used to levitate microdroplets for measurements, will be presented in this chapter.

2.2 The Lorenz-Mie theory: scattering by spherical particles

As already mentioned by Bohren and Huffman [4] the mathematics of electromagnetic waves scattering by a spherical particle, presented by Mie in his 1908 paper [5], is straightforward and so is the expansion of the electromagnetic fields into infinite series, representing the field at all points in space. Visualization of the fields and categorization of the important/excited electromagnetic modes inside and outside the spherical scatterer is cumbersome. Though there are several methods or reformulations of this problem [9][10][27][31][40][82], the Mie theory presented by [4] (in chapter 4 of his book) will be followed. However, only the equations relevant to this study will be derived or considered, while being careful to couple experimental/practical considerations and assumptions when necessary. In other words, this approach represents the shortest route to obtain a physical solution to the problem as applied to this study while referring interested readers to the complete and chronological deductions of the formal solution.

2.2.1 Solutions to the vector wave equations using vector spherical harmonics

In relation to this study, consider a spherical particle (microdroplet) of arbitrary size (radius) a_{d} and refractive index m_{d} illuminated by a time-harmonic plane electromagnetic field ($\vec{E}$, $\vec{H}$), such that the $\vec{E}$ field is polarized parallel to the z-axis. By standard convention, the $\vec{H}$ field is orthogonal to the $\vec{E}$ field and the wave is propagating towards the positive y-axis. In accordance with the LMT and for practical applications, the microdroplet is generally assumed to be spherical, isotropic, homogeneous and embedded in non-absorbing medium (free-space is usually assumed). It is further desirable (for this specific application) that the material of such microdroplet is optically linear – thus its response/polarizability does not depend on the strength of the incident field. In this case, the fields propagating in free-space satisfy the wave equation (or the Helmholtz equation) given as:

$$\left.\begin{aligned}\nabla^2\vec{E}+k_{\mathrm{s}}{}^2\vec{E}=0\\ \nabla^2\vec{H}+k_{\mathrm{s}}{}^2\vec{H}=0\end{aligned}\right\} \qquad (1)$$

Where k_{s}, is the wave number in the surrounding medium (or free-space) and $k_{\mathrm{s}}{}^2=\omega^2\varepsilon\mu$, ε and μ being electric permittivity and magnetic permeability constants respectively. Also, the field outside and inside the microdroplet must satisfy Maxwell's equations:

$$\left.\begin{aligned}\vec{\nabla}\bullet\vec{E}&=0\\ \vec{\nabla}\bullet\vec{H}&=0\end{aligned}\right\}$$
$$\left.\begin{aligned}\vec{\nabla}\times\vec{E}&=i\omega\mu\vec{H}\\ \vec{\nabla}\times\vec{H}&=-i\omega\varepsilon\vec{E}\end{aligned}\right\} \tag{2}$$

The next task in this derivation is to define two vector harmonic functions $\vec{M}$ and $\vec{N}$ from a scalar function ψ (called a generating function) and constant vector (guiding vector), such that, both $\vec{M}$ and $\vec{N}$ satisfy the above requirements. With the earlier assumption of a spherical microdroplet, it is understood that there exists symmetry in the problem at hand, hence the choice of a scalar function ψ, which satisfies the wave equation in spherical polar coordinates is evident. The less obvious choice is the guiding vector. The popular choice is an arbitrary constant vector $\vec{C}$, as done by [4] to show that both $\vec{M}$ and $\vec{N}$ satisfy the above equations, before settling on the radius vector as the guiding vector. In the same spirit of the latter choice of the radius vector $\vec{r}$, both $\vec{M}$ and $\vec{N}$ may be written as:

$$\left.\begin{aligned}\vec{M}&=\left(\vec{r}\psi\right)\\ \vec{N}&=\frac{\vec{\nabla}\times\vec{M}}{k_s}\end{aligned}\right\} \tag{3}$$

Granting that $\vec{M}$ is a solution to the vector wave equation and ψ is also a solution to the scalar wave equation, both of them being in spherical polar coordinates, the problem is reduced to finding the solutions to the scalar wave equation given by:

$$\frac{1}{r^2}\frac{\partial}{\partial r}\left(r^2\frac{\partial\psi}{\partial r}\right)+\frac{1}{r^2\sin\theta}\frac{\partial}{\partial\theta}\left(\sin\theta\frac{\partial\psi}{\partial\theta}\right)+\frac{1}{r^2\sin\theta}\frac{\partial^2\psi}{\partial\phi^2}+k_s{}^2\psi=0 \tag{4}$$

The separation of variable approach produces solutions of the form: $\psi(r,\theta,\phi)=R(r)\Theta(\theta)\Phi(\phi)$ which, when substituted into equation (4), gives the following equations:

$$\frac{d^2\Phi}{d\phi^2}+m^2\Phi=0 \tag{5}$$

$$\frac{1}{\sin\theta}\frac{d}{d\theta}\left(\sin\theta\frac{d\Theta}{d\theta}\right)+\left[n(n+1)-\frac{m^2}{\sin^2\theta}\right]\Theta=0 \tag{6}$$

$$\frac{d}{dr}\left(r^2\frac{dR}{dr}\right)+\left[k_s{}^2r^2-n(n+1)\right]R=0 \tag{7}$$

where m and n are the separation constants. The final step towards constructing generating functions ψ that satisfy equation (4) involves obtaining solutions to each of these equations (5) – (7), by application of independent secondary conditions that ψ must satisfy. These sec-

ondary conditions have been extensively discussed by [4] leading to the construction of the following *even* (*e*) and *odd* (*o*) generating functions:

$$\psi = \begin{cases} \psi_{emn} = \cos m\phi P_n^m(\cos\theta) z_n(k_s r) \\ \psi_{omn} = \sin m\phi P_n^m(\cos\theta) z_n(k_s r) \end{cases} \tag{8}$$

Where $\cos m\phi$ and $\sin m\phi$ are the linearly independent solutions of equation (5), with *m* taking positive integer values. The functions $P_n^m(\cos\theta)$, for $n = m, m + 1, \ldots$ are the Legendre functions of the first kind (of degree *n* and order *m*) which are solutions of equation (6) and are finite at $\theta = 0$ and $\theta = \pi$. Finally, the functions $z_n(k_s r)$ are any of the four spherical Bessel functions $j_n(\rho)$, $y_n(\rho)$, $h_n^{(1)}(\rho)$ or $h_n^{(2)}(\rho)$ (see section 4.1 of [4] for details) which are the solutions to equation (7) after the following transformation; $\rho = k_s r$ and $Z = R\sqrt{\rho}$.

The consequence of such generating functions, as defined in equation (8), is that the generated vector spherical harmonics (defined in equation (3)) can be rewritten by substituting ψ_{emn} and ψ_{omn} to obtain the corresponding four vector spherical harmonics; $\vec{M}_{emn}$, $\vec{M}_{omn}$, $\vec{N}_{emn}$ and $\vec{N}_{omn}$.

2.2.2 Expanding the incident plane wave and the scattered fields in vector spherical harmonics

Now, consider the earlier assumption an *x*-polarized plane wave $\vec{E}_{\text{inc}}$ must be written in spherical polar coordinates as: $\vec{E}_{\text{inc}} = E_o \exp(ik_s r\cos\theta)\hat{e}_x$,

where $\hat{e}_x = \sin\theta\cos\phi\hat{e}_r + \cos\theta\cos\phi\hat{e}_\theta - \sin\phi\hat{e}_\phi$.

Expanding $\vec{E}_{\text{inc}}$ in vector spherical harmonics using $\vec{M}_{emn}$, $\vec{M}_{omn}$, $\vec{N}_{emn}$ and $\vec{N}_{omn}$, and multiplying each by an appropriate coefficient (A_{emn}, A_{omn}, B_{emn} and B_{omn}) it may be written as:

$$\vec{E}_{\text{inc}} = \sum_{m=0}^{\infty}\sum_{n=m}^{\infty}(B_{emn}\vec{M}_{emn} + B_{omn}\vec{M}_{omn} + A_{emn}\vec{N}_{emn} + A_{omn}\vec{N}_{omn}) \tag{9}$$

The reader is encouraged to refer to section 4.2 of [4] for the step-by-step procedure to obtain the expansion coefficients. Though the possible values of *m* and *n* have already been stated above, it was shown during this derivation that only $m = 1$ suffices, since all $m \neq 1$ coefficients vanish, and after the determination of the expansion coefficients, the incident electric field can be written as:

$$\vec{E}_{\text{inc}} = E_o\sum_{n=1}^{\infty} i^n \frac{2n+1}{n(n+1)}(\vec{M}_{o1n}^{(1)} - i\vec{N}_{e1n}^{(1)}) \tag{10}$$

Where the superscript (1) in equation (10) indicates that $z_n(k_s r) = j_n(k_s r)$ is the appropriate spherical Bessel functions to be used in the generating function (compare equations (3) and

(8)) for the incident wave because they are the only finite functions at the origin. Then by taking the curl of equation (10), the corresponding incident magnetic field is obtained (see equation 4.38 in [4]). The field inside the spherical scatterer and the scattered field can be determined in a similar fashion as expressed above. However, the orthogonality property of vector spherical harmonics and the appropriate boundary conditions must be applied, if the form of equation (10) must be obtained. The boundary condition in this case is $(\vec{E}_{inc}+\vec{E}_{scat}-\vec{E}_{\text{int}})\times\hat{e}_r=(\vec{H}_{inc}+\vec{H}_{scat}-\vec{H}_{\text{int}})\times\hat{e}_r=0$. Since the scattered fields are of interest in this study, they are expressed as:

$$\begin{aligned}\vec{E}_{scat}&=E_o\sum_{n=1}^{\infty}i^n\frac{2n+1}{n(n+1)}(ia_n\vec{N}_{e1n}^{(3)}-b_n\vec{M}_{o1n}^{(3)})\\ \vec{H}_{scat}&=\frac{k_{\text{s}}}{\omega\mu}\sum_{n=1}^{\infty}i^n\frac{2n+1}{n(n+1)}(ib_n\vec{N}_{o1n}^{(3)}+a_n\vec{M}_{e1n}^{(3)})\end{aligned}\tag{11}$$

In this case the superscript (3) in equation (11) indicates that $z_n(k_{\text{s}}r)=h_n^{(1)}(k_{\text{s}}r)$ is the appropriate asymptotic spherical Hankel functions to be used in the generating function for the scattered fields at large distances of $k_{\text{s}}r\gg n^2$. They represent outgoing spherical waves or scattered waves, in other words. The final step is to derive expressions for the scattering coefficients a_n and b_n, an endeavour that has again been comprehensively carried out by [4]. The final expressions have been written as:

$$\begin{aligned}a_n&=\frac{m_{\text{r}}\psi_n(m_{\text{r}}x_{\text{d}})\psi_n'(x_{\text{d}})-\psi_n(x_{\text{d}})\psi_n'(m_{\text{r}}x_{\text{d}})}{m_{\text{r}}\psi_n(m_{\text{r}}x_{\text{d}})\xi_n'(x_{\text{d}})-\xi_n(x_{\text{d}})\psi_n'(m_{\text{r}}x_{\text{d}})}\\ b_n&=\frac{\psi_n(m_{\text{r}}x_{\text{d}})\psi_n'(x_{\text{d}})-m_{\text{r}}\psi_n(x_{\text{d}})\psi_n'(m_{\text{r}}x_{\text{d}})}{\psi_n(m_{\text{r}}x_{\text{d}})\xi_n'(x_{\text{d}})-m_{\text{r}}\xi_n(x_{\text{d}})\psi_n'(m_{\text{r}}x_{\text{d}})}\end{aligned}\tag{12}$$

Where $x_{\text{d}}=k_{\text{s}}a_{\text{d}}=2\pi m_{\text{s}}a_{\text{d}}/\lambda$ and $m_{\text{r}}=k_{\text{d}}/k_{\text{s}}=m_{\text{d}}/m_{\text{s}}$ are respectively, the size parameter and the relative refractive index, computed from the wave number in the droplet's surrounding medium, k_{s}, and in the spherical microdroplet k_{d}, the droplet radius a_{d}, refractive index of the microdroplet m_{d} and of the surrounding medium m_{s}. These final expressions are obtained by introducing the Riccati-Bessel functions $\psi_n(\rho)=\rho j_n(\rho)$ and $\xi_n(\rho)=\rho h_n^{(1)}(\rho)$ while the primes indicate the first differentials with respect to the arguments.

2.2.3 Scattering matrix and the scattered intensities

In practice, experiments are carried out by measuring the far-fields, usually at large distances of $k_{\text{s}}r\gg n^2$ (a condition which has already been fulfilled in the expansion of the scattered fields). Another condition that needs to be fulfilled is the convergence of the terms of equation (11) for sufficiently large n to allow for the termination of the series expansion with small error in $k_{\text{s}}r$. Scattering in any chosen direction has been described by four complex amplitude functions, S_1, S_2, S_3 and S_4, which are functions of θ and ϕ. They form the four ele-

ments of the matrix $S(\theta,\phi)$ (known as the scattering matrix) [4][9]. Generally, the scattered electric field is related to the incident electric field through the scattering matrix as:

$$\begin{pmatrix} E_{scat,\theta} \\ E_{scat,\phi} \end{pmatrix} = \frac{e^{ik_s(r-z)}}{-ik_s r} S(\theta,\phi) \begin{pmatrix} E_{inc,\theta} \\ E_{inc,\phi} \end{pmatrix} = \frac{e^{ik_s(r-z)}}{-ik_s r} \begin{pmatrix} S_2 & S_3 \\ S_4 & S_1 \end{pmatrix} \begin{pmatrix} E_{inc,\theta} \\ E_{inc,\phi} \end{pmatrix} \tag{13}$$

For spherical particles, which is the case for the LMT, $S_3 = S_4 = 0$. Consequently, equation (13) reduces to two complex amplitude functions. The end result is that the transverse components of the scattered electric field can be expressed as:

$$\begin{aligned} E_{scat,\theta} &\sim E_o \frac{e^{ik_s r}}{-ik_s r} \cos\phi S_2(\cos\theta) \\ E_{scat,\phi} &\sim E_o \frac{e^{ik_s r}}{-ik_s r} \sin\phi S_1(\cos\theta) \end{aligned} \tag{14}$$

The expressions for the scattering amplitudes functions S_1, and S_2 can be found in section 4.4.4 of [4]. The intensity functions of the polarized scattered light (vertically I_V and horizontally I_H), in other words, phase functions due to their angular dependence are finally written as;

$$\begin{aligned} I_V &= \left|E_{scat,\perp}\right|^2 = \frac{\lambda}{4\pi r^2}|S_1|^2 \\ I_H &= \left|E_{scat,\parallel}\right|^2 = \frac{\lambda}{4\pi r^2}|S_2|^2 \end{aligned} \tag{15}$$

In Figure 2.1 the theoretical intensity patterns are represented for a microdroplet of diethylene glycol (DEG) with radius of 15 µm, refractive index of 1.4455 which is illuminated with a plane wave of wavelength 658 nm. In practice, it can be realized when such a microdroplet sits in the waist of a loosely-focused laser beam – the variation of the light intensi-

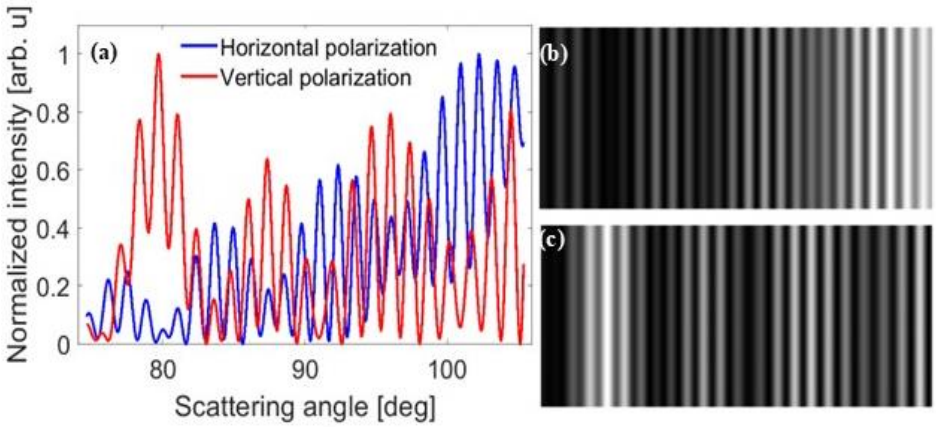


Figure 2.1: Theoretical intensity patterns for a microdroplet of DEG with radius of 15 µm, refractive index of 1.4455 which is illuminated with a plane wave of wavelength 658 nm. The horizontal and vertical polarizations have been presented in (a). Their corresponding images for an angle of elevation of -5 – 5° are presented in (b) and (c) respectively.

ty over the droplet would be negligible and the wave-front is flat there. The normalized intensities for horizontal and vertical polarizations have been presented alongside their respective images for observation angle range of 74 – 105° and angle of elevation of -5 – 5°.

2.3 The speckle phenomenon

We start with a model of a diffusive medium which contains an infinitely large collection of spherical scatterers with the same optical properties (refractive index, diameter and uniform reflectivity or transmissivity), but randomly distributed in the medium. Their random distributions, consequently, impose random phases in relation to an incident light and the observation screen. In the case of solid surfaces, only phase change between -π and +π is equally possible upon scattering [45], [47], [49]. While in a medium, as assumed, all phase changes with respect to the incident are equally likely. Applying the "*random walk in the complex plane*" model, we consider the bright regions in the speckle pattern as coming/originating from isolated scattering areas. The contribution of a scatterer (located at a point $Q(u, v, w)$ in the medium) to the light at a point $P(x, y, z)$ on the observation screen is denoted by $\Phi_{uvw}(x, y, z; t)$. For laser illuminations which are usually monochromatic, this contribution takes the form

$$\Phi_{uvw}(x,y,z;\ t) = A_{uvw}(x,y,z)\exp\left[\frac{i2\pi}{\lambda}(ct - r_{uvw}) + \varphi_{uvw}\right] \tag{16}$$

Where $A_{uvw}(x, y, z)$ is the amplitude of the field, φ_{uvw} is the random phase angle associated with the scatterer at $Q(u, v, w)$, λ is the wavelength of the laser, c is the speed of light and r_{uvw} is the distance between points $Q(u, v, w)$ and $P(x, y, z)$ expressed as:

$$r_{uvw} = \left[(x-u)^2 + (y-v)^2 + (w-z)^2\right]^{\frac{1}{2}} \tag{17}$$

Here (w – z) is the perpendicular distance between the scatterer in the medium and the observation screen. If another scatterer, located in the vicinity of point $Q(u, v, w)$ – denoted as $Q'(u + \delta u, v + \delta v)$ – must contribute a similar field (as in equation (16)) to the same point $P(x, y, z)$ to produce constructive or destructive interference, the interference conditions must be obeyed. However, for such a large collection of scatterers randomly distributed in the volume of the medium (sending out random wavelets), the common analytical approach is the sum of either the phasor amplitudes [44] or intensities [51] of the contributions from many scatterers. The complex-valued phasor amplitude can be separated from equation (16) as:

$$\beta_{uvw}(x,y,z) = A_{uvw}(x,y,z)\exp\left[i\theta(x,y,z)\right] \tag{18}$$

where $\theta(x,y,z) = (-2\pi/\lambda)r_{uvw} + \varphi_{uvw}$, and the total amplitude from N scatterers that would contribute to the point $P(x, y, z)$ is expressed as:

$$\beta(x,y,z) = \sum_{k=1}^{N}\left|a_k(x,y,z)\right|\exp\left[i\theta_k(x,y,z)\right],\ k = 1,2,3,\ldots,N \tag{19}$$

Where $a_k(x, y, z)$ are the amplitudes of each phasor contribution. Now, by introducing the properties of the scatterers such that each occupies an infinitesimally small volume, $\Delta u \Delta v \Delta w$. The power density, which is incident on the medium is $G(u, v)$. Each scatterer, receiving direct illumination from the incident laser, will attenuate an amount α upon scattering [51]. Also, choosing the real part of equation (19), it can be rewritten as:

$$\beta(x,y,z) = \left[\frac{\alpha G(u,v)\Delta u \Delta v}{\pi r^2}\right]^{\frac{1}{2}} \cos\left(\frac{-2\pi}{\lambda} r + \varphi_{uvw}\right) \tag{20}$$

The intensity measured in experiments may be expressed from equation (16) or (19) as if we let $\sum_{k=1}^{N} |a_k(x,y,z)| = |a(x,y,z)|$:

$$\begin{aligned} I(x,y,z;\, t) &= \lim_{t \to T} \int_{-T/2}^{T/2} \left|\Phi(x,y,z;\, t)\right|^2 dt \\ &= \left\langle \beta(x,y,z) \cdot \beta^*(x,y,z) \right\rangle = \left|a(x,y,z)\right|^2 \end{aligned} \tag{21}$$

Where T is the camera's integration or light collection time. A careful look at equation (19) suggests that when the concentration of scatterers increases, more scatterers will be present to contribute to the amplitude at a single point on the observation screen depending on their phase relationships. In practice, this phenomenon (increase in intensity) is usually observed when the concentration of scatterers is increased. However, there is no known explicit expression between the intensity variation and concentration changes except the derivation of average intensity, variance and consequently, the probability density function in the statistical analysis [45], [47], [49],[51]. The probability density function, (reported to follow negative exponential trend [44]) expresses the probability of finding intensity I from the speckle pattern produced by a large number of scatterers. It is worth emphasizing that there is a $1/\sqrt{N}$ factor appearing in some derivations of equation (19) in literature (compare earlier publication of Goodman [45] to later ones [48]) – though highly debated by Lord Rayleigh in a series of publications prior to Goodman's [49], [50]. All the above derivations may be applied to static scatterers in the medium (in which case $I(t)$ = *constant* for each point resulting in static speckle pattern) or moving scatterers resulting in dynamic speckle pattern.

Consider the two media (colloidal suspensions) investigated in this study, the "*bulk medium*", 10 µL of cow milk (of different fat content/concentration) in a 50 µm thin cuvette [81] and "*microdroplet medium*", different sizes (from ~ 125 to 30 µm) of microdroplets containing monodisperse inorganic nanoparticles. An analogous investigation of the "*bulk medium*" consisting of nanoparticles in thin cuvette was performed earlier [80] as well as the many reports of analysis of dynamic speckles in literature. Such dynamic speckle patterns recorded over a period of time will consist of frames/images, each representing a moment in time of the combination of several scatterers to produce each bright region in the pattern.

2.3.1 Light scattering by microdroplets of colloidal suspension ("*microdroplet medium*")

As discussed above, random scattering of light by a suspension occurs when there is density and/or refractive index fluctuation, or random distribution of the particles in the medium. However, in a spherical microdroplet of suspension which is freely levitating in a gaseous medium, the two light scattering regimes (from first principle) that may be encountered are: scattering by the spherical microdroplet as a whole and scattering by the system of particles located in the microdroplet's medium. Hence, the purpose of this subsection is to illustrate these scattering regimes with simple discussions/analyses rather than detailed or rigorous mathematical derivations as presented by many authors [41], [83], [84], [85]. In other words, the analysis presented here only represents an approximate distinction between light scattering by a spherical microdroplet as a whole and the system of particles located in the microdroplet medium.

Experimental studies of optical sizing and evaporation-driven aggregations of microdroplets of pure liquids and colloidal suspensions have been reported earlier by our group [42], [86], [87], [88], [89] and others [21], [56]. Notable examples of samples include silica, gold, titanium oxide, gadolinium oxide nano-spheres, and sodium dodecyl sulphate micelles/nanostructures in water, glycols and other liquids. Specifically, A. Wozniak et al., [42] did not only present scanning electron microscopy (SEM) images of microdroplets of suspensions soft-landed on a surface at various stages of the evaporation, but also numerical simulations for comparison. The initial evolution stages of their droplets were characterized by a high population of inclusions in the interior with few partly appearing on the surface. Later stages, however, were characterized by increase in the population of inclusions on the surface until the formation of a highly-ordered surface layer of inclusions and then a dried-up nanoparticle aggregate. These effects, in general, depend on the hydrophobicity or hydrophilicity of the inclusions, their Brownian motions or migration to and/or from the surface and most importantly the shrinking of the droplet's surface layer due to evaporation.

Now the detail of the categories already presented in the problem statement: (i) scattering from the spherical microdroplet (where LMT can be applied as discussed in section 2.2 and was applied by many authors [42], [86], [87], [88], [89]) and (ii) scattering from the inclusions as an ensemble of scatterers (where the speckle phenomenon can be applied as discussed in section 2.3) will be discussed. In the first category of scattering, the Mie scattering patterns can be measured with a well-designed optical setup such that the influence from the inclusions will be very minimal. Detailed experimental considerations will be presented in chapter 3 with special attention to evaporating droplets of suspensions. Thus, in cases where almost all the inclusions are located in the interior/volume of the droplet with only a few appearing on the surface but not enough to cause surface roughness, the Mie scattering patterns can be well measured.

In the second category (also requiring a different well-designed optical setup, see chapter 3) the microdroplet simply serves as a spherical micro-cuvette. Though containing a minute number of inclusions, their speckles patterns can still be measured. However, the use of the so-called *structure factor* analysis (as presented by several authors [84], [90]), to describe: the structure of the system (scattering regime), the length scale of scattering and the inclu-

sions/scatterers' separations may not be feasible due to the following reasons, stated for simplicity in the language or ray optics:

(i) the scattering wave vector, $\vec{q}_{\mathrm{wv}} = \vec{k}_{\mathrm{sc}} - \vec{k}_{\mathrm{in}}$ which is defined as the change in momentum between incident ($\vec{k}_{\mathrm{in}}$) and scattered ($\vec{k}_{\mathrm{sc}}$) field momenta respectively cannot be directly known because the droplet's surface curvature greatly modifies the incident beam through either single or multiple internal reflections and refractions before reaching the inclusions. This also means that the scattering wave vector defined in any scattering experiment as $q_{\mathrm{wv}} = (4\pi/\lambda)\sin(\theta/2)$, (where λ is the wavelength and θ is the scattering angle between incidence and scattering directions) does not directly apply.

(ii) the *structure factor*, expressed as $S_f(\vec{q}_{\mathrm{wv}}) = \sum_{i,j}^{N} e^{i\vec{q}_{\mathrm{wv}}\bullet(\vec{r}_i - \vec{r}_j)}$ [84], [90] (where N is the number of inclusions in the microdroplet volume, $\vec{r}_i$ and $\vec{r}_j$ are the positions of the *i*- and *j-th* inclusions respectively), the *i*- and *j-th* inclusions (at certain distance of separation) may be "illuminated" by different internal caustics orientated differently by the curvature of the droplet surface.

Hence in both media where speckle patterns are measured, neural network will be used as an efficient model for statistical pattern recognition and classification [70]. This is because, in the final activation function of the neural network used here (see below), the probability of each speckle pattern belonging to each class will be computed using Bayes' theorem. Consequently, each pattern will be classified to the class with the highest probability. Thus, speckle patterns which are recorded from the same sample are expected to have similar statistics/probabilities which will only change considerably with change in the parameters of the samples.

2.4 Convolutional neural networks: theoretical background

Due to the wide varieties/types of neural networks (a few already presented in chapter 1) – though similar in some cases – the theoretical background pertaining to the type used in this study will be presented here. The multilayer feed-forward convolutional neural network was used throughout this study. Convolutional neural networks were initially built for processing image data (both 2D and 3D) [91],[92], nowadays however, convolutional networks have been used for time series (audio and video) and vector sequence input processing [93]. They have a unique property of being invariant to some transformations of the input data [70],[71]. For example, an object or human face photographed is invariant upon translation, scaling and in some cases small rotations. Hence, creating sufficiently large data set with multiple invariant transformations (such as reported by [94] and references therein) and using a fully connected network (neurons are fully connected) has been demonstrated to be the simplest way to achieve such network invariance, since the network learns from data.

A 35-layer CNN was used from the beginning which was later modified to 41 layers capable of handling more classes and larger data set (see chapter 3 for details). The first two layers of the network can be modelled using a set of M input variables $x_1, \ldots, x_M$ as [70]:

$$y_k(\vec{\mathrm{X}}, \vec{\mathrm{W}}) = \xi\left[\sum_{j=1}^{N_L} w_{kj}^{(2)} f\left(\sum_{i=1}^{M} w_{ji}^{(1)} x_i + w_{j0}^{(1)}\right) + w_{k0}^{(2)}\right] \tag{22}$$

Thus the first layer, denoted by the superscript $^{(1)}$, is a linear combination of the input variables multiplied by weights, $w_{ji}^{(1)}$ plus biases $w_{j0}^{(1)}$ and transformed using a nonlinear activation function $f(\bullet)$. The output of this first layer (a nonlinear function) then becomes the input for the next layer, where new set of weights and biases are applied. In all, except the final, layers of the network used in this study, the rectified linear unit (ReLU) was applied as the activation function. Before the final output to the network, a suitable activation function, which is determined by the data and type of the output variables must be chosen. As can be inferred from equation (22), this activation function is different from the one used in the earlier layers (also known as hidden units) of the network. The *softmax activation* function $\xi(\cdot)$ was chosen for the multiclass classification problem in this study to enable the Bayesian or probabilistic interpretation of the output. The final output $y_k(\vec{\mathrm{X}}, \vec{\mathrm{W}})$ is then a function of the input and weight vectors respectively and k = 1, 2, 3, …, K, where K represents the total number of final outputs (number of classes in our case). In general, the features are extracted from the data (images) by performing convolution (using convolution kernels or filters) and since information gets passed from earlier layers to later ones (forward propagation), hence the name feed-forward neural networks.

2.4.1 The final activation and error functions

As outlined in chapter 5 of [70], and in relation to the choice (or otherwise) of suitable final activation function and an error function, neural networks may be used to solve three main types of problems. Standard regression tasks involve linear combinations of inputs, weights and biases without an activation function, the sum-of-squares error is the appropriate error function to be minimized. In the second type of problem (binary and multiple-independent binary classification), the logistic sigmoid activation function is used to produce nonlinear outputs. Then, as demonstrated by Simard *et al*. [95], the cross-entropy error function leads to a shorter training time and improved generalization capabilities. The final type of problem (as in this study) involves a multiclass classification in which the classes are mutually exclusive. However, since classification tasks generally uses labels as outputs/targets instead of numerical values as used in regression tasks, a target-label to numerical coding scheme must be used [70],[96]. For example, consider a total of K mutually exclusive classes (k = 1, 2, …, K), resulting from a set of input and target vectors $(\vec{\mathrm{X}}, \vec{t})$ respectively, the target-label t_k belonging to a class k may be coded as:

$$t_k = \begin{cases} 1, & \text{For class } k \\ 0, & \text{All other classes} \end{cases}$$

In this case, the *softmax* (or normalized exponential) is applied (immediately after a fully connected layer) as the final activation function, whose output is probabilistic and may be expressed as; $\xi(\bullet) = y_k(\vec{X}, \vec{W}) = p(t_k = 1|X)$. This is the posterior probability (or conditional probability) which is obtained through Bayes' theorem [70] and expressed in terms of the class-conditional and prior probabilities $p(X|t_k)$ and $p(t_k)$ respectively as:

$$p(t_k = 1|X) = \frac{p(X|t_k)p(t_k)}{\sum_j p(X|t_j)p(t_j)} = \frac{\exp(a_k)}{\sum_j \exp(a_j)} \tag{23}$$

and $a_k = \ln p(X|t_k)p(t_k)$. The multiclass cross-entropy error function is the appropriate error function (see details in [70],[96]). This probabilistic interpretation of the network output is the most suitable approach for the statistical analysis of the speckle pattern recorded from the suspensions.

With a general view of the neural network for multiclass classification as a nonlinear function constructed from a set of input and output vectors, parameterized by adjustable weights (which include the biases), its training involves minimizing the error function by finding the optimum weight vector (see [70],[96] for details).

2.4.2 Convolutional neural network architecture

In Figure 3.7, a plot of the convolutional neural network architecture is presented showing all layers as nodes. Unlike the nomenclature suggested by [70] where only layers in which inputs data get modified are counted, we simply adopt the nomenclature used in MATLAB for easy reference. A detailed description of the network architecture will be presented in the related

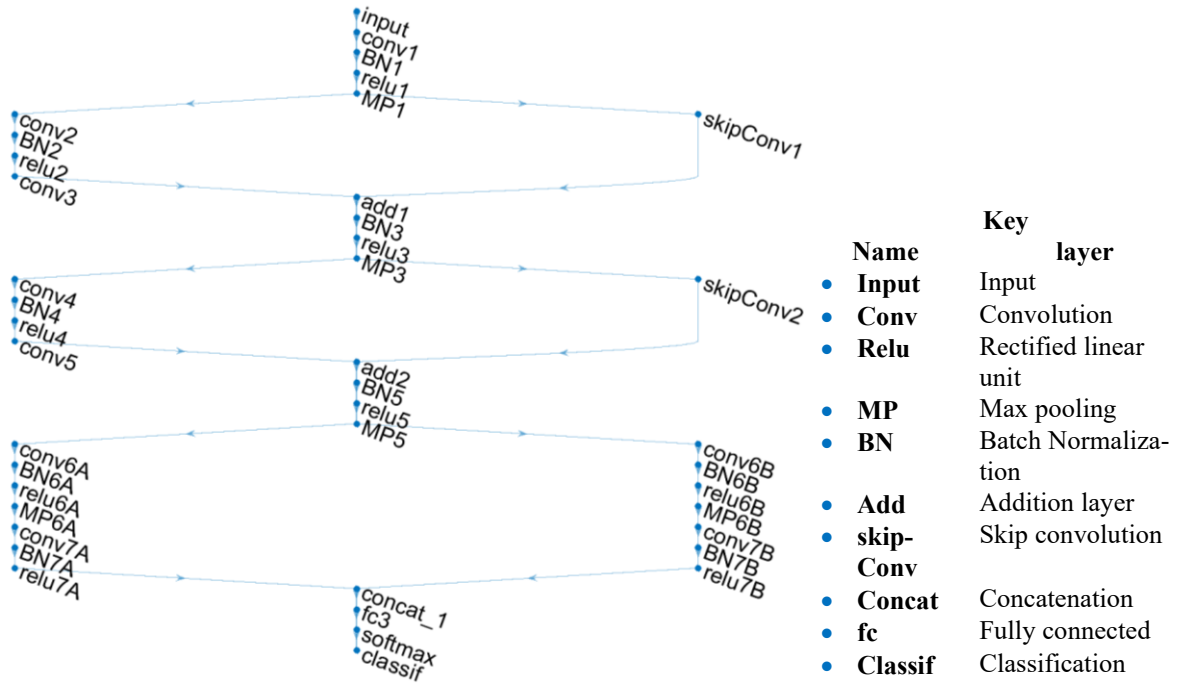


Figure 2.2: A plot of the network's architecture, showing network layers as nodes and interconnections. See description in the publication (chapter 4).

publication (see chapter 4) while a detailed analysis of one of the trained networks, provided by MATLAB's network analyser will be presented in Appendix. The analyser provides the total learnable parameters and detail parameters of each layer/node.

2.5 Electrodynamic particle levitation

As already outlined in chapter 1, trapping and levitating of single/multiple particles enables the verification of light scattering theories and, ultimately, the use of optical techniques or a combination of them for particle characterization. It offers the possibility to observe/measure scattering in the near-forward direction [97], rainbow angle [98], around 90° angle [99], [100] and other directions or solid angles [60]. The movement of a non-weightless, charged particle in an alternating quadrupole electric field can be perceived as the motion of a particle in a pseudopotential (electric interactions + inertia) with a minimum. The motion can be described with the so called Mathieu equations [101]. Though the theory and basic principles are universally the same as reported almost 100 years before the first invention of the device as a mass filter by Paul and Steinwedel [102], we will follow the derivation of Wolfgang Paul as presented in his (Nobel Prize in Physics) lecture [59].

The Paul traps are generally categorized into two- or three-dimensional based on the field configuration in the trap. The quadratic potential of the electric quadrupole field in Cartesian coordinates is expressed as:

$$\Phi = \frac{\Phi_o}{2r_o^2}(\alpha x^2 + \beta y^2 + \gamma z^2) \tag{24}$$

where r_o is the distance from the centre of the trap to the electrode. When the Laplace condition ($\Delta\Phi = 0$) is applied, it is evident that the sum of the coefficients must equal zero $(\alpha + \beta + \gamma = 0)$ to satisfy this condition. The field configuration can then be generated. Since there exist two general ways to satisfy this equation, we consider the first case, where $(\alpha = 1 = -\gamma,\ \beta = 0)$. Then equation (24) reduces to

$$\Phi = \frac{\Phi_o}{2r_o^2}(x^2 - z^2) \tag{25}$$

This generates a two-dimensional field (see [59] for field configuration). By applying a combined DC voltage U and an AC voltage V of frequency ω, the amplitude in equation (25) is given by $\Phi_o = U + V\cos\omega t$, and the equations of motion of the particle in the trap are expressed as:

$$\begin{aligned} \ddot{x} + \frac{e}{mr_o^2}(U + V\cos\omega t)x = 0 \\ \ddot{z} - \frac{e}{mr_o^2}(U + V\cos\omega t)z = 0 \end{aligned} \tag{26}$$

In the second case, $\alpha = \beta = 1,\ \gamma = -2$, in which case equation (24) is expressed as:

$$\Phi = \frac{\Phi_o (r^2 - 2z^2)}{r_o^2 + 2z_o^2} \tag{27}$$

This results in a three-dimensional field configuration (see [59] for field configuration). Similarly, the equations of motion are:

$$\begin{aligned} \ddot{x} + \frac{e}{mr_o^2}(U + V\cos\omega t)x &= 0 \\ \ddot{y} + \frac{e}{mr_o^2}(U + V\cos\omega t)y &= 0 \\ \ddot{z} - \frac{2e}{mr_o^2}(U + V\cos\omega t)z &= 0 \end{aligned} \tag{28}$$

Where e and m are the electric charge and mass, respectively, of the particle in the trap. The time-dependent terms of the force obtained from these equations of motion of the particle in a homogeneous field will equal zero upon averaging. On the contrary, in a quadrupole field (which is inhomogeneous and periodic), there is always an average force (though small) directed toward the centre where the field is small [103].

Now, we employ the Mathieu equations in dimensionless form;

$$\begin{aligned} \frac{d^2x}{d\tau^2} + (a + 2q\cos 2\tau)x &= 0 \\ \frac{d^2y}{d\tau^2} + (a + 2q\cos 2\tau)y &= 0 \\ \frac{d^2z}{d\tau^2} - 2(a + 2q\cos 2\tau)z &= 0 \end{aligned} \tag{29}$$

The coefficients a, q and τ can be found in relation to the particle properties and the trapping field by comparing equation (29) with either equation (28) or (26) depending on the field configuration used in trapping. Thus,

$$a = \frac{4eU}{mr_o^2\omega^2},\ q = \frac{2eV}{mr_o^2\omega^2},\ \tau = \frac{\omega t}{2} \tag{30}$$

Stability in the trap depends exclusively on the a and q parameters, irrespective of the initial parameter of the motion of the charged particle, e.g. velocity. Stability diagrams of a vs q for both 2D and 3D field configuration have been plotted and explained in detail by [59][104]. Apart from the factor of 2 appearing in equation (27) and/or (28) for the 3D field which causes the field in the z-direction to be stronger, the charged particles perform the same motion in both field configurations. Thus, in both field configurations, the most relevant region within the stability diagram is $0 < a, q < 1$, through which an operating line (a/q = *constant*) can be drawn when r_o, ω, U and V remain constant. In view of equation (30), all charged particles

with the same *m/e* will be located at the same point in the stability region, while different masses will be located at different points on the operating line.

Since the invention by Paul, there have been several reports of different experimental setup designs or configurations of traps in literature. For example geometries similar to Paul's – made up of four hyperbolically/cylindrically shaped rod-electrodes arranged strategically in a quadrupole configuration [59], [42], [105], [106]. A similar configuration made of four stainless steel electrodes arranged vertically but with an attached 60^{o}-angle branching electrodes (known as branched quadrupole trap) was reported by [107]. The configuration allows the simultaneous dispensing of two different substances for chemical reaction to take place in the trap. There are also the double ring geometry [60], [67], hyperboloidal geometry made up of a ring electrode and two end-cap electrodes [59], [101], [103], [108], [109], cubic geometry, made of six flat electrodes arranged into a hollow cube [110], and others [111]. A different geometry reported by [112] consists of four tubes, pairs of which have the same dimensions. The smaller tubes (inner-electrodes, 3 mm outer diameter) were separately mounted into the larger tubes (outer-electrodes, 8 mm inner-diameter) such that, when arranged vertically with a 4 mm air-gap between the outer-electrodes, the inner-electrodes will be separated by an 8 mm air-gap. This geometry, as demonstrated, provides a 360^{o} view of the trapped droplet in the horizontal plane [112], and a flow of gas through the tubes.

It must, however, be emphasized that there exist other trapping techniques, for example, in the Penning trap [113] a magnetic field is applied alongside the electric field which can be used to trap single atoms, electrons, and neutrons [59], [114].

In this study we have used both the cylindrically shaped rod-electrodes (the 2D-trap) and a geometry made up of a hollow, top-flat, doughnut-shaped middle electrode and two end-cap electrodes (the 3D-trap, see Figure 2.2). These traps were built in our lab and developed over several years with several variants for research [103], [105], [115]. The assembled and dis-assembled earlier variant of the 3D-

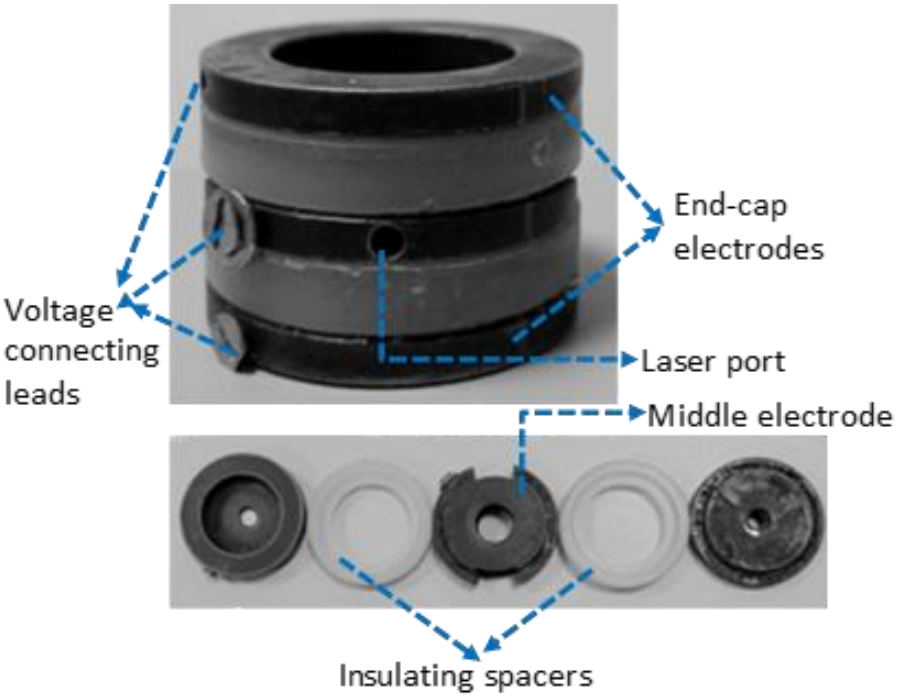


Figure 2.3: An earlier variant of the 3D electrodynamic trap, assembled (top panel) and dis-assembled (bottom panel). The middle electrode shows ports for both 90^{o} and 270^{o} view of the trap interior or droplets.

trap is presented in Figure 2.2, showing fewer ports. This geometry creates much smaller volume of quadrupole field than a true hyperboloidal trap. The current modifications of the 3D-trap specific to this study will be presented partly in chapter 3 and partly in our publication (which will be reproduced in chapter 4) while the modifications of the 2D-trap will be presented in chapter 3.

Chapter 3
Experimental Methods

3.1 Chapter overview

Considering the foundation that has been laid already in both Chapters 1 and 2, the three separate experimental methods carried out will be presented in this chapter. In the case where the results have been published, a summary of the experimental method and aspects not covered in the related publication will be presented with citations when necessary.

3.2 Recognition of concentration-driven speckle changes from the "*bulk medium*" of a real-world suspension (milk)

As stated in chapter 2, theoretically, the fundamental relation which can be used to analyse the change in concentration and its effect on the intensity is equation (19). However, practically, the difficulty in differentiating between speckle patterns taken from samples with different concentrations lies in a number of reasons. Firstly, the total number of scatterers, N, contributing to a chosen bright area cannot be determined. Specifically for moving scatterers, all future N contributions to this and any other chosen area are nondeterministic. Secondly, the irregular width, lengths and positions of these isolated bright areas appearing on the whole pattern present a large-scale detailed structure that cannot be easily distinguished by any analytical method. It must, however, be emphasized that though the speckle size – the statistical average of the distance between adjacent regions of maximum brightness – may be determined, it does not relate to the concentration of scatterers.

Beside the above reasons, there is a well-known phenomenon that, lower concentrations of samples produce weak intensities while higher concentrations cause the intensity maxima to exceed the camera's dynamic range leading to overexposure. Though it is always beneficial to use a camera with high dynamic range but the recording of speckle patterns from multiple sample concentrations with the same exposure time does not allow fully developed speckle pattern to be recorded from each sample. Since the most probable intensity in a fully developed speckle pattern is zero [44].

There are however other features like higher statistical momenta, speckle shape, fine features, pixel co-occurrence, etc., originating e.g. from multiple scattering which increases with concentration, but which are not easily attributable or recognizable as attributable to concentration, but may be learned by a neural network.

In convolutional neural network environments, all the information processed by previous layers may be passed on to the subsequent layers without image dimensionality reduction, though it requires higher computational resource. On the other hand, gradually reducing the image dimension by taking the maximum value from each section of the image that the convolutional kernels are applied (known as *Maxpooling*) or computing the average of each image after convolution (known as *Globalpooling*) have been shown to be very effective in network training and classification while requiring less computational resource.

Hence in the first study, we used convolutional neural network to recognize speckle patterns generated from milk samples of different fat contents (concentration) as well as investigated

multiple scenarios of speckle recording and network training. The results and finding were presented in a full research article and published in European Physical Journal Plus. With permission from the journal, the article will be presented in Chapter 4.

3.3 Droplet sizing and tracking of evaporating microdroplets of pure liquids, liquid mixtures and suspensions

In the second study, the aim was to use convolutional neural network to recognize the sizes of single (but different) droplets levitating in a quadrupole electrodynamic trap. This head-on approach would involve injecting size-tailored droplets from a droplet injector, choosing the right trapping parameters for trapping each droplet and generating a large dataset (of measured Mie scatting patterns) for training the neural network. As will be discussed below, this approach poses significant problems at each stage of the process. Hence an established alternative method of injecting, trapping, balancing and evaporating single droplets was implemented while generating theoretical dataset to train the convolutional neural network. This approach is more advantageous and feasible to implement since a wide and continuous range of droplet sizes is covered during each evaporation. Furthermore, larger theoretical dataset can be generated for network training and a wider range of radii can be covered as opposed to trapping single droplets of different sizes.

3.3.1 The trap, levitation of droplets and evaporation

The quadrupole electrodynamic trap used in this study was in-lab built and used extensively with several modifications (see [115], [116]). The geometry discussed in chapter 2 was built (see Figure 3.1) and ports were created for laser and white-light illuminations, cameras views, and temperature/humidity sensor. A top port was created for the injector while the bottom port allows the observation of the larger volume of the trap than the side ports. Top and bottom ports also double as the venting ports for filling/flushing the trap chamber with dry nitrogen. The trap was kept in a climatic chamber and held in place at the top and bottom by two insulating rings. The air-gap between the trap and climatic chamber walls and the many ports enable the flow of dry nitrogen gas through the chamber and the trap. Since tubes with dark internal coatings were connected between the cameras and the chamber, it can be considered as an isolated or closed chamber with no external light interference. There is also minimal atmospheric influence – the chamber was loosely

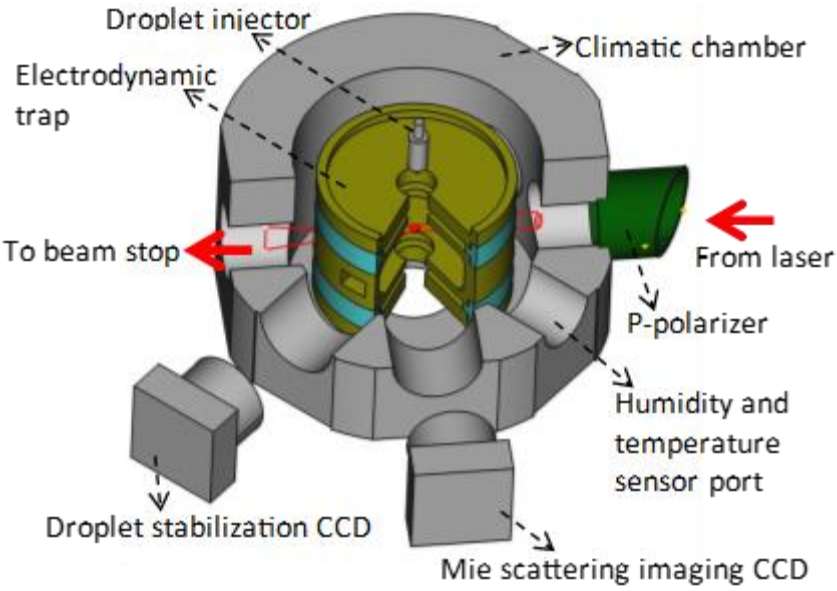


Figure 3.1: A schematic diagram of the 3D setup for measuring Mie scattering pattern from microdroplets.

sealed so that the slight internal overpressure quickly equalized with the ambient atmosphere.

As demonstrated by Wolfgang Paul using the stability diagram, droplet trapping and levitation (also known as balancing) is only possible when its mass-to-charge ratio falls within the stability region (see Figure 2 and 7 in [59] or Figures 5 – 7 in [101]). For an evaporating droplet, the AC field (used for trapping) and the DC field (used for trapping and balancing its weight) must be continuously adjusted to keep it in the pseudo-potential minimum of the trap.

Typically, the droplet still undergoes a slow secular oscillatory motion (with a frequency $\omega_o = \beta\omega/2$) which is modulated with a faster oscillatory micro-motion (at the frequency of the AC field) [59]. As shown by Wolfgang Paul a ratio between these two frequencies can be used as a criterion for stability selection. Critical values of this ratio permit that the displacement made by the micro-motion averages out over a period of the oscillatory secular motion. However, in this experiment the droplet stabilization was achieved by a proportional-integral-derivative (PID-type) feedback loop which strives to keep the droplet in the "ground state" of the trap, practically suppressing any secular motion. The working mechanism of the PID-type feedback loop has been reported in multiple publications [87], [105].

The trap construction, as described above, also allows for temperature control and stabilization. Hence, by choosing the appropriate temperature and humidity, the droplet can be made to evaporate under different conditions (see examples [117], [118], [119]). The droplets were injected into the trap using a droplet-on-demand injector.

3.3.2 Droplet injector design and injection

The droplet-on-demand injector used in the study is an in-lab built injector – a skill that has been developed over time, producing multiple variants (see earlier publications [42], [103], [105]). It was produced by melting the lower end of a fused silica microcapillary tube (mounted vertically on a rotating motor (15 rps)) with a jeweller's gas-oxygen micro-burner. The melted lower end of the capillary then extended downward, due to gravity action, forming an internally tapered capillary tube. It was then polished on fibre optic polishing films to an exit orifice (nozzle) diameter of ~50 μm. The capillary was finally glued into a wired piezoelectric tube (PTYY-0118, PI Ceramic GmbH). After vacuum drying, the injector can be filled with liquid or suspension through a syringe and a flexible silicon tube pulled onto the untampered end of the capillary.

The injector was mounted on the top-port of the climatic chamber with its nozzle extending downwards to the top end-cap electrode of the trap (see Figure 3.1). The piezoelectric transducer was driven with a short bipolar electrical pulse for droplet injection. Typically, single droplet can be produced by a careful investigation of the amplitude and pulse duration of the electrical pulse versus the liquid's inertia, viscous force, surface tension and droplet pinch-off mechanisms (see [120], [121] and reference therein). Droplet size control may also be achieved by a careful choice of these parameters but the injector nozzle diameter greatly dictates the size range that can be produced [121]. In this study, however, on average multiple droplets are produced during each injection so that by scanning the trapping field, a single droplet (with the right mass-to-charge ratio) may be trapped. While the remaining droplets

simply escape the trapping field due to instability. Also, multiple pulse-signal amplitudes ranging between 50 and 400 V and duration ranging between 10 and 30 µs were applied to achieve droplet size control and/or injection of different liquids/suspensions. Droplet charging was done mainly by charge separation upon exiting the injector nozzle into the external field. External charging using a high voltage O-ring electrode mounted in front of the injector nozzle is also applied in some cases.

Hence, due to the above reasons and the fact that droplet mass and charge are not fully controllable during injection and not all injections result in successful trapping of droplets, it was not feasible to perform experiments with size-tailored droplets. For example, trapping size-tailored single droplets in each experimental run which could eventually be composed into a well-defined droplet-size variation was not feasible. On the contrary, trapping single droplets and evaporating them will ensure that a wide range of radii would be covered for the purpose of this investigation.

3.3.3 Sample preparation

The samples were made up of: (i) pure diethylene glycol (DEG, 0.99 purity, BioUltra, GC, Fluka), (ii) a liquid-liquid mixture of dipropylene glycol, (0.99 purity, mixture of isomers, Alfa Aesar) and distilled water in volume ratio of 6:4 (DPG:H_2O), two suspensions of low concentration: (iii) a mixture of diethylene glycol and monodispersed aqueous suspension of polystyrene microspheres, in volume ratio of ~9:1 (DEG:PS) and (iv) a mixture of dipropylene glycol and monodispersed aqueous suspension of silica nanospheres, further diluted with distilled water to a final volume ratio of ~5:4:1 (DPG:H_2O:SiO_2). The suspensions were prepared by mixing and ultrasonication. The refractive indices of all the pure liquids were measured in a separate study and reported in our publications [122], [123]. The diameter of the PS microspheres (2.5 wt% in manufactured suspension, SIGMA) was 1.1 µm, refractive index ≅ 1.59. The diameter of SiO_2 nanospheres (5 wt%, Corpuscular Inc.) was 450 nm and refractive index ≅ 1.465.

3.3.4 Experimental considerations and measurement of Mie scattering patterns

As stated in chapter 2, the LMT presupposes illumination with a plane wave. In this experiment with a coherent laser beam, a plane wave was mimicked by a flat wave-front in the beam waist, achieved by passing a beam through an imaging lens [124] which creates a 1 mm beam waist (diameter) at the centre of the trap. Then considering a 30 µm droplet located at this not-tightly-focused beam waist, it can be assumed to be illuminated with a broad parallel beam (or plane wave).

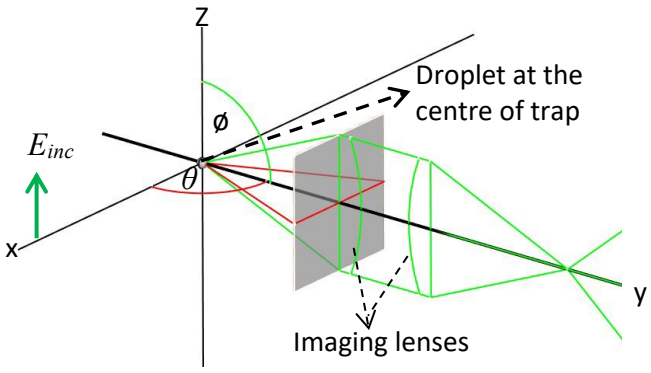


Figure 3.2: A schematic diagram (not drawn to scale) of the droplet at the centre of the trap and a confocal imaging system projecting Mie scattering patterns onto a CCD (not shown).

As depicted in Figure 3.2 the confocal optical system was used to project

the Mie scattering patterns – centred on the 90 ± 15.40° angle (azimuth) and ±5° angle of elevation – onto the CCD. The setup (purposely designed for droplet sizing) enables the measurement of well resolved Mie scattering patterns (see Figure 3.3 (a) and (b)) from microdroplets of pure liquids. Such well resolved Mie scattering patterns will enable the comparison of theoretically generated pattern with the experimentally recorded ones leading to the accurate sizing of the microdroplets and tracking of the radius evolution during their evaporation.

In the case of microdroplets of suspensions, the Mie scattering patterns can still be recorded but with a minimal influence of the colloidal particles on the internal fields at this point of observation. Now we focus on the case of evaporating microdroplets of suspensions as introduced in chapter 2. Figure 3.3 (c) and (d) represent the Mie scattering patterns recorded from the initial and final stages (respectively) of evaporation of a microdroplet of suspension of PS in DEG. The influence of the colloidal particles manifests as irregular and short-lived distortions of the internal fields which can be observed in the Mie scattering patterns (see the dashed-orange oval in Figure 3.3 (c)). These distortions get significantly more pronounced when the droplet is getting to the end of evaporation where a solid aggregate is obtained. These distorted patterns appear to take the structure of speckles, however, they are much broader (see Figure 3.3 (d)) as compared to the speckle size that would have been obtained if the same suspension were illuminated in a (thin) cuvette as we showed earlier [81]. Compare also the speckle patterns recorded from a microdroplet of suspension at a different observation point (see the next section) with Figure 3.3 (d). Their maxima also seem to coincide with the maxima (or centres) of the original Mie scattering pattern.

As a part of the scattering process, transparent droplets produce bright spots (also known as glare points [125]) near their edges. It has been shown by both geometrical optics approximations and LMT that the glare points are formed from the exit points of rays which are reflected and/or refracted into those points [125]. Their intensities are several orders of magnitude higher than the rest of the Mie scattering patterns. Further detailed analysis of glare points and their application can be found in the literature – typically in laser interferometric measurements [126], [127] for large droplet and bubble sizing [128], [129] as well as tracking [61], [62],

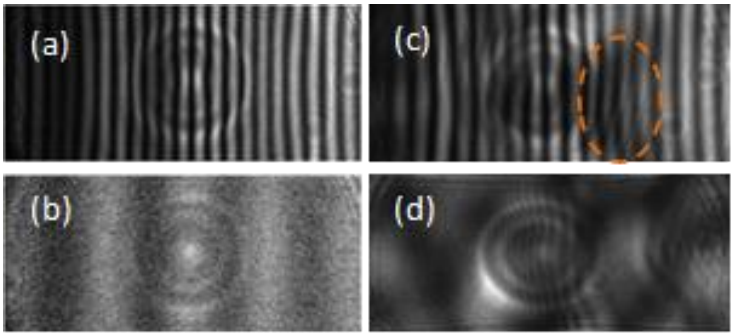


Figure 3.3: Well-resolved Mie scattering pattern recorded from evaporating microdroplets of: pure DEG ((a) and (b)) and suspension of SiO_2 in DEG ((c) and (d)). The scattering patterns measured at the beginning (a) and (c) and at the end (b) and (d) of evaporation are shown. The distortions caused by the nano-particle(s) to the field in the droplet which manifests on the Mie scattering pattern is indicated by the orange oval in (c). The effect is enhanced towards the end of evaporation (d). The difference in the signal-to-noise ratio between (b) and (d) is due to the fact that pure droplets can evaporate to much smaller sizes than suspensions.

[127].

However, the practical measurements of Mie scattering patterns are often achieved by setting up a telescope to zoom into a small solid angle thereby cutting off the glare points and allowing only the low-intensity part of Mie scattering patterns to be measured. In this experiment, the glare points fall well outside the field-of-view defined by the observation geometry.

Since movies of the Mie scattering patterns were recorded over the entire evolution of each trapped droplet, the measurement enabled the tracking of the temporal evolution of the microdroplets of the samples. Further details of laser illumination, data recording and extraction, theoretical data generation, grouping and labelling as well as network architecture, training and result analysis have been discussed in a publication which will be reproduced in chapter 4.

3.4 Parameter-driven speckle changes from microdroplets of suspensions

Now we focus on the second category of scattering as introduced in chapter 2. The general aim here is to measure scattering/speckle from the inclusions/scatterers in the microdroplets medium, so that changes in the parameters of the suspension can be used to recognize and classify the suspension. However, as discussed above, the optical system and the point of observation allowed Mie scattering from the spherical microdroplets to be measured with only minimal influence from the scatterers. Since the "footprint" of scattering from the scatterers was not very distinct, a different optical system was necessary. It must, however, be emphasized that a further modification of the optical system in Figure 3.2 and change in observation point could have allowed the measurement of these speckle patterns from the inclusions. Nonetheless, a design of an optical system which can be coupled with a linear trap (already in use) was easy and allowed both setups to be used concurrently.

Figure 3.4 represents the linear trap geometry with the coupled optical system (see [42] for details of the first variant). The trap geometry consisted of four cylindrically shaped rod-electrodes. The four rod-electrodes (86.65 mm long and diameter 4.75 mm) were strategically arranged and held together (at the top and bottom) by two 3D-printed holders. The rods then formed a square pattern with 4.80 mm distance of separation along the sides. This configuration was carefully fitted into a hollow metallic cylinder (75.65 mm long) acting as a shield (which in turn was fitted into a 3D-printed climatic chamber, not

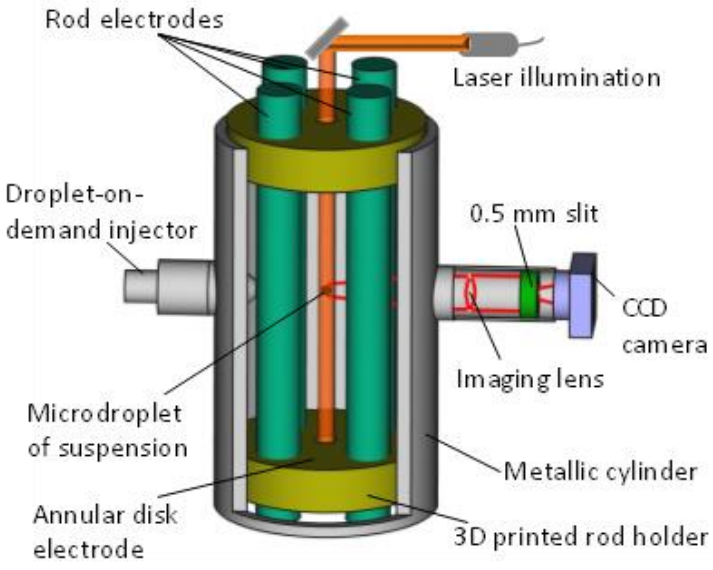


Figure 3.4: A schematic diagram of the 2D trap for measuring speckle patterns from microdroplets of suspensions.

shown). A 10 kV (AC) voltage was applied to the diagonal pairs of the rod-electrodes. The frequency of the voltage ranged from 100 to 700 Hz, depending on the mass-to-charge ratio of the droplet. In this case, the charged microdroplet is confined horizontally to a small volume but can still move along the vertical axis of the rod-electrodes.

Its vertical motion was constrained by two disc-electrodes with circular bores on the trap axis (carefully insulated from the four rod-electrodes), mounted at the inner sides of the two 3D-printed holders and driven with DC voltage. The configuration of the disc-electrodes used produces a field with a gradient (rather than a uniform one), and thus it was possible to shift the point at which the DC field counteracts the gravity action along the vertical axis, thus freely moving the droplet along this direction. Obviously, the DC voltage used depends on the trapped droplet mass-to-charge ratio.

The ports for laser illumination were created at the centre of both 3D-printed holders while ports for both injector and camera were created across the centre-most part of the metallic cylinder. A 15 mm focal length imaging lens was mounted at 20 mm from the trap producing a magnified image of the droplet such that the speckles from the nanoparticles, around a 90^{o} angle to the illumination direction, can be registered on the CCD. A combination of factors such as trap volume and weak scattering intensity from the nanoparticles, the influence of higher intensities from the droplet's glare points and the inverse relation between the speckle size and aperture (slit) diameter dictated the recording of optimum speckle size at a longer distance of 420 mm from the lens. A 0.5 mm slit was used to cut off the higher intensities from the glare points on the droplets.

Its current state permits the measurement of scattered light from the colloidal particles distributed in the volume of the microdroplet. Since these measurements falls under the speckle phenomenon, as discussed in previous chapters, two parameter-driven speckle changes were investigated as outlined in the problem statement. Microdroplets of different concentrations of colloidal suspensions (see Figure 3.5 for speckle patterns measured from 10 and 50 mg/ml and compare with Figure 3.3) and the same concentration but different sizes of microdroplets were measured. The neural network was trained for recognition and classification (more speckle patterns and results will be presented in chapter 4).

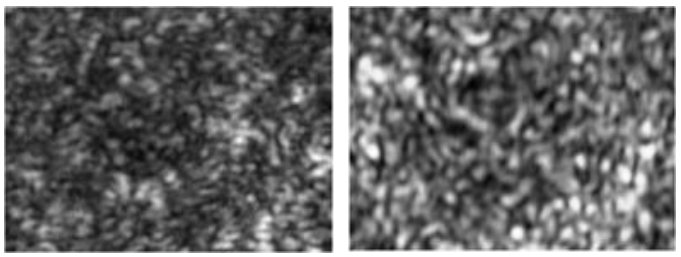


Figure 3.5: Speckle pattern recorded from microdroplets of suspensions of two different concentrations, 10 mg/ml (left panel) and 50 mg/ml (right panel). Compare the speckle patterns at this observation point with Figure 3.3.

3.4.1 Concentration-driven speckle changes

In the concentration-driven speckle changes measurements, approximately equal sizes of microdroplets of suspensions were produced but from different concentrations (5, 10, 20 30 and 50 mg) of Gd_2O_3 :1% Nd nanoparticles (ø = 305 nm, the doping with Nd is of no importance for these measurements, while the high refractive index of ~2 enables bright speckles) in

DEG. When a droplet is trapped and balanced, it is illuminated vertically with a green laser (wavelength = 532 nm) and the speckle patterns are recorded using a colour camera (Pike F-032C, AVT, working in 8-bit mode). For each droplet, exactly 1000 images were recorded with exposure time of 10 ms. Since it was not possible to simultaneously measure Mie scattering pattern from this setup, an alternative method of droplet sizing (shadowgraphy [130]) was used to estimate the droplet size. It was achieved by recording the shadows of the droplets within the time frame of measuring 1000 images. This procedure was repeated for each concentration mentioned above.

The 640 × 480 images were normalized to 0 – 1 grayscale level and the network was trained in a classification task with a randomized selection of 8:1:1 for the training, test and validation sets respectively.

3.4.2 Size-driven speckle changes

In this measurement, the droplet injector was not operating in a single droplet mode. When the voltage amplitude and pulse duration used to drive the injector were varied, groups of droplets with different size distribution were generated and then a single droplet was selected by tuning the trapping AC/DC parameters. This allowed measuring droplet of somewhat different sizes. As illustrated in Figure 3.6, since different sizes of droplets were produced from the same concentration, the changes in speckles will only occur as a result of the number of scatterers in the droplets or the viewing volume. Here the analysis presented by Bruning and Lo [41], involving two spherical particles system may be employed to explain the many possible scenarios of scattering. For example, the scenario in which two spherical inclusions are aligned parallel to the direction of illumination or perpendicular to the observation direction (with broadside illumination) or such alignment alike may be encountered. Furthermore, scenarios in which each inclusion is in each other's far-field or in near-field are possible. The difference, however, lies in the number of inclusions considered as well as the size of the viewing volume. In this study, microdroplets of suspensions of sizes (diameter) ranging from ~124 down to ~35 μm were trapped and their speckle patterns were recorded. As mentioned above the speckle patterns recorded were analysed using convolutional neural network.

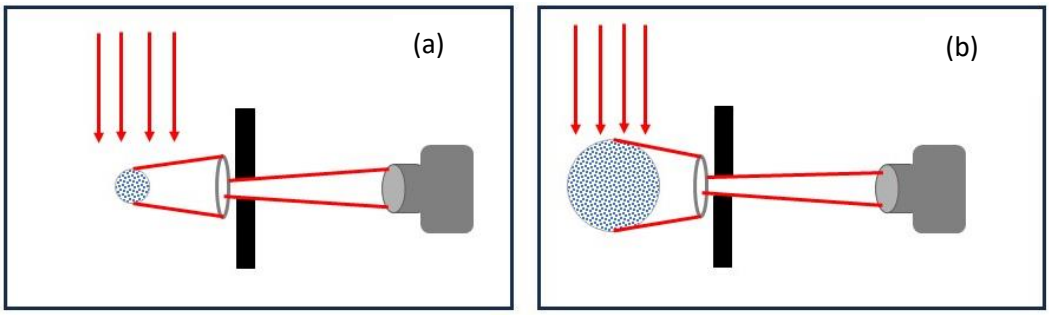


Figure 3.6: A 2D illustration of the size-driven speckle changes. The small droplet (a) will contribute less scatterers as compared to the big droplet (b).

Chapter 4
Results and Discussions

4.1 Chapter overview

In this chapter, the results obtained from the separate investigations carried out will be presented in three parts as outlined in the problem statements. The results and findings obtained from the first two investigations have already been published. Hence, in Part I and Part II the copies of the publications (reproduced with permission) will be preceded by the publication's metadata (title, online resource and summary). Additional data and unpublished results (if any) will be added as supplementary results under separate subsections. In Part III, the unpublished results of the last investigations will be presented and discussed in full, with relevant citations (if any). Finally, a comparison between some aspects of the *"bulk"* and *"microdroplet"* media will be presented.

Part I

4.2 Investigation of parameters of suspensions in the *"bulk medium"*

Publication title: "*Combining transmission speckle photography and convolutional neural network for determination of fat content in cow milk: an exercise in classification of parameters of a complex suspension*"

The PDF version of this publication has been reproduced below, with permission from The European Physical Journal Plus (as stated on their web page [131]). The online version may be accessed from [81].

4.2.1 Supplementary materials in online data repository

Sample videos, extracted images and all the trained networks are available online at external data repository (Mendeley Data) [132].

4.2.2 Summary of publication

In a 10 mm (circular diameter) by 50 μm thin cuvette (which was built in the lab) the parameters of complex milk suspensions (*bulk medium*) were investigated. Movies of the transmitted speckles from these suspensions were recorded at different camera's exposure-time protocols and a convolutional neural network was trained using the two available training options (ADAM and SGDM). The network was successfully trained in a classification task and the optimum exposure-time protocol and network training option were chosen for further investigation and validation. All results were confirmed with both test and independent data sets. Detailed explanation of the investigation is presented in the publication as reproduced below.

4.2.3 A copy of the published article

Part II

4.3 Classification of radius evolution and tracking the evaporation rate of microdroplets of pure liquids and suspensions

Publication title: "*A convolutional neural network technique for online tracking of the radius evolution of levitating evaporating microdroplets of pure liquids, liquid mixtures and suspensions*"

The PDF version of this publication has been reproduced below, with permission from The Journal of Quantitative Spectroscopy and Radiative Transfer [133]. The online version may be accessed from [134].

4.3.1 Supplementary materials in online data repository

Sample experimental images, generated images and the trained networks are available online at external data repository (Mendeley Data) [135].

4.3.2 Summary of publication

In this study, theoretical Mie scattering patterns were generated (and grouped into classes of small ranges of radii) for evaporating microdroplets of pure liquids, liquid-liquid mixtures and suspensions. A convolutional neural network was trained on the generated data and the trained network was used to classify, sequentially, experimentally recorded Mie scattering patterns from evaporating microdroplets. The freely evaporating droplets were levitated in a quadrupole electrodynamic trap during measurements. The microdroplets were produced from: (i) pure diethylene glycol, (ii) a suspension of diethylene glycol and monodispersed aqueous solution of polystyrene microspheres, (iii) a mixture of dipropylene glycol and distilled water and (iv) a suspension of dipropylene glycol, distilled water and monodispersed aqueous solution of silica nanospheres. The preparation of samples has been described in chapter 3 and in the publication. The study enabled the tracking of the temporal radius evolution of microdroplets of pure liquids, liquid-liquid mixtures and suspensions with entry-level accuracy.

4.3.3 A copy of the published article

4.3.4 Supplementary results (unpublished)

Mie scattering patterns were measured from multiple droplets and the trained networks were used to classify their patterns sequentially as stated in the publication. The measured but unpublished results will be presented in this section. These results include additional droplets recorded from:

(i) pure diethylene glycol (DEG)
(ii) diethylene glycol and polystyrene suspension (DEG + PS)
(iii) dipropylene glycol and distilled water mixture (DPG + H_2O) and
(iv) dipropylene glycol, distilled water and silica suspensions (DPG + H_2O + SiO_2).

(i) Supplementary results for pure DEG

Figure 4.1 represents supplementary results for two microdroplets of pure DEG. The Stage 1 network (see publication) was used to classify images from Droplet 3 and Stage 2_2 network was used to classify images from Droplet 4. In each case the network was chosen based on the initial radius of the droplet and the data was classified sequentially. These supplementary results validate the robustness/stability of the technique and the network over multiple measurements. As can be seen in Figure 4.1 the *main-branch* of evaporation curves can be traced from the beginning to the end of evaporation. However, both curves seem to show spread of data points due to initial contamination with moisture causing the change of refractive index of the droplet. This effect, as discussed in the publication, manifests in the spread of points (see the dashed-orange circles in Figure 4.1). The region indicated by the dashed-green circle in the evaporation curve of Droplet 3 may again be attributed to factors like the change of refractive index due to increased content of impurities, which have already been discussed in the publication. Another factor that may be responsible for discontinuities of the *main-branch* or the spread of data points, worth

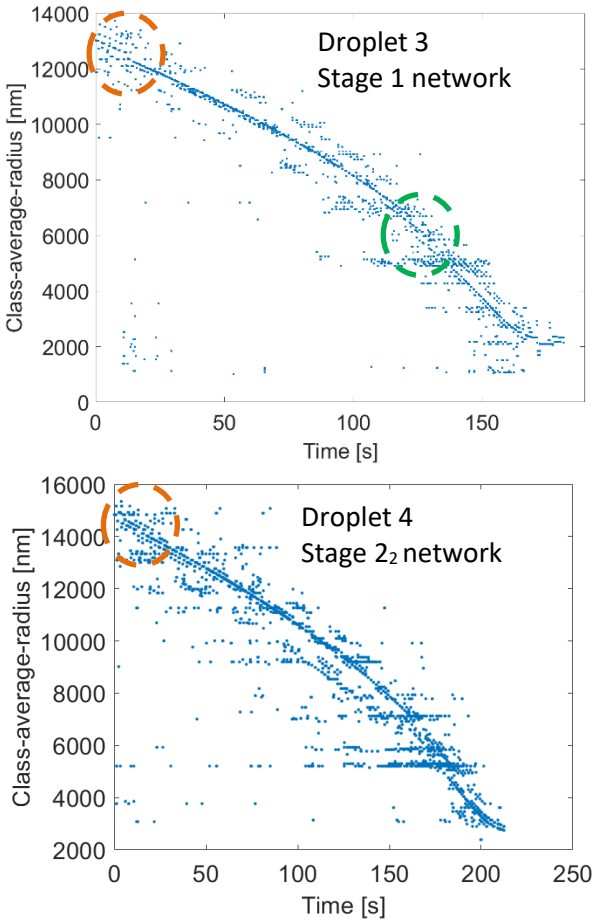


Figure 4.1: Classification of experimental Mie scattering patterns recorded from two microdroplets produced from pure DEG (see publication for Droplets 1 and 2). The networks used for classification were chosen based on initial droplet radius. The dashed-orange circles at the beginning of each curve indicate contamination with moisture. The spread of points indicated by the dashed-green circle may be attributed to several factors discussed in the publication.

emphasizing here, is the minute variation (uncertainty) of the droplet's position within the trap. Droplets of suspension are particularly prone to it, since the stabilization loop using the distorted image of the droplet yields more noise in stabilizing DC voltage, while droplets are confined to relatively small volumes and the field may not be perfectly quadrupolar. Small movements of the droplet result in small shifts of the Mie pattern, which are then misinterpreted by the method.

(ii) Supplementary results for DEG + PS

In Figure 4.2, the supplementary results have been presented for two microdroplets of DEG + PS suspension. In both cases there are multiple branches of possible evolution and a significant spread of points. Considering these results and the results presented in the publication, it seemed that, for microdroplets of suspensions, the choice of the refractive index of the highest constituent produced multiple branches of evaporation (see the publication for details). Hence, two methods were applied/tested to find an optimal refractive index (which will represent an effective value for all the constituents of the suspension under study). Firstly, the method of fitting theoretical scattering patterns to experiment (as done for pure DEG) was applied to DEG + PS data. The refractive indices, radii of droplets and temperatures at which the generated data fits to experimental data were physically meaningful and compatible with the experimental conditions (see fit in Figure 4.3).

However, after training on such data, the classification did not only produce multiple branches of evaporation but also multiple discontinuities. Figure 4.4 represents a classification of the droplets presented in Figure 4.2 using a network trained on such fitted data (with refractive index of 1.4425, droplet initial radii radius of 12695.6 nm and a temperature of 21±0.2°C at which evaporation was carried out, see Figure 4.3). While this problem may still be attributed to the choice of parameters, it may also likely be caused by the distortions of the internal fields of the droplets by the inclusions which manifest on the Mie scattering patterns, as discussed in chapter 3. So that fitting only produces physically meaningful parameters because mean scattering vectors are com-

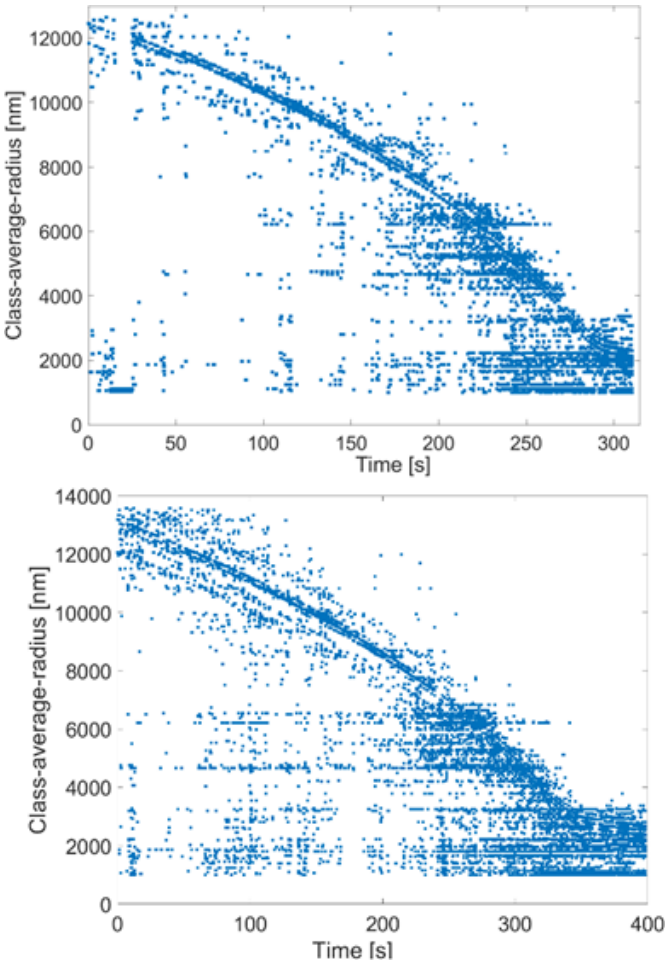


Figure 4.2: Classification of experimental Mie scattering patterns recorded from two evaporating microdroplets of DEG + PS suspension. Here the refractive index of DEG was used during data generation since it was the highest constituent.

puted from the images during fitting while the distortions are still present during image classification. Secondly, the volume ratio (of DEG and the aqueous solution of PS) was used to calculate the effective refractive index but again, training on such data did not produce any improvement in the results either. It appears that, surprisingly, the presence of the suspended phase does not affect the effective refractive index of the microdroplet strongly enough to significantly alter the fundamental Mie scattering pattern. The changes to the scattering pattern seem to come mostly as a coherent addition from scattering on the (nano)particles of suspended phase.

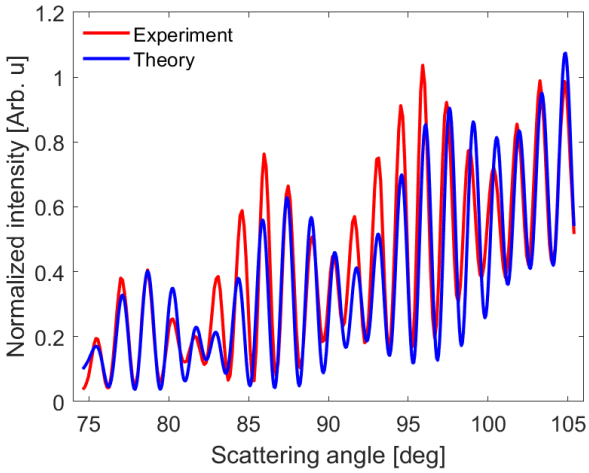


Figure 4.3: A fit of Mie theory to experimental light scattering pattern recorded from a microdroplet of suspension of polystyrene in diethylene glycol at droplet radius of 12695.6 nm, refractive index of 1.4425 and a temperature of 21±0.2°C.

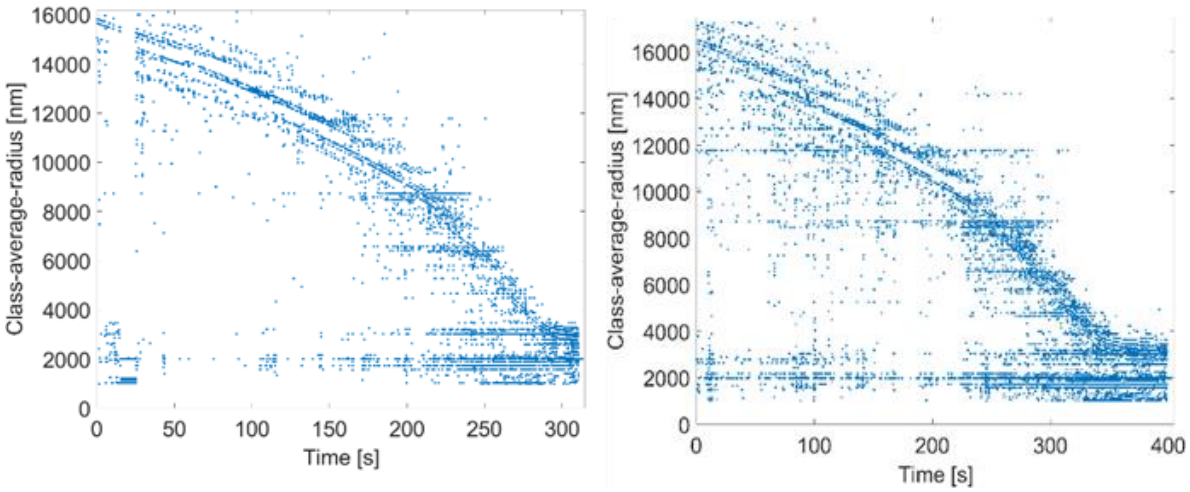


Figure 4.4: A reclassification of the droplets presented in Figure 4.2 using a network trained on data generated after fitting Mie theory to experiment. These results of fitting were compared with the results in Figure 4.2 where the refractive index of DEG was used for training the network.

(iii) Supplementary results for DPG + H_2O

The result of classification of two different microdroplets recorded from a binary mixture of DPG and H_2O is presented in Figure 4.5. As can be seen there are multiple branches of evaporation which seem to have improved as compared to Figure 9 in the publication. The trend is maintained in both cases with relatively fewer points widespread. Here, it appears that liquid water fraction is already in equilibrium with the atmosphere in the trap chamber in accordance with the predictions of the evaporation model [117]. The highly volatile liquid (water) evaporated rapidly at the beginning (not registered here) until equilibrium is reached, after which the microdroplet composition changed slowly. The influence of non-volatile or low-volatility impurities is again evident in the observed slowdown of evaporation.

(iv) Supplementary results for DPG + H_2O + SiO_2

The supplementary results for two microdroplets have been presented in Figure 4.6. These droplets are rather small compared with that presented in the publication and seem to produce very high classifications. Nonetheless, there are still multiple branches of evaporation (indicated by the orange arrows) and overlapping discontinuities (indicated by dashed-green circles) in Figure 4.6. Interestingly, it can be observed in this figure and in Figure 10(b) of the publication that the method fails once the concentration of SiO_2 particles reaches approximately a 30-fold increase relative to the initial concentration at injection. In contrast, for the PS suspension (Figure 4.2 and Figure 10(a) in the publication), even a ~100-fold increase in concentration does not cause the method to fail – the cessation of radius decrease toward the end of the evolution can still be observed. This can probably be traced to different inclusions distribution evolution for SiO_2 vs PS, leading to different distortion manifestation (refer to Figure 3.3 (d)). This has been partly studied e.g. in [87]. Indeed, though the mixing ratio of both SiO_2 and PS were the same in their separate suspensions (see section 2 in the publication), the size difference (d_{SiO2} = 0.45 µm and d_{PS} = 1.1 µm) may have very well contributed to the effect. The droplet of SiO_2 suspension will contain more particles than that of PS.

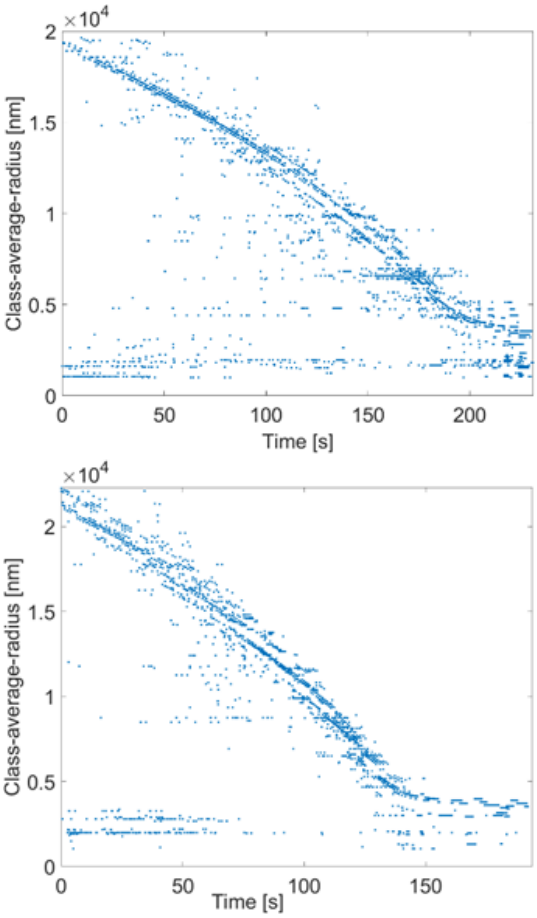


Figure 4.5: Classification of experimental Mie scattering patterns recorded from two microdroplets of DPG + H_2O mixture. The network described in section 4.3 of the publication was used for classification.

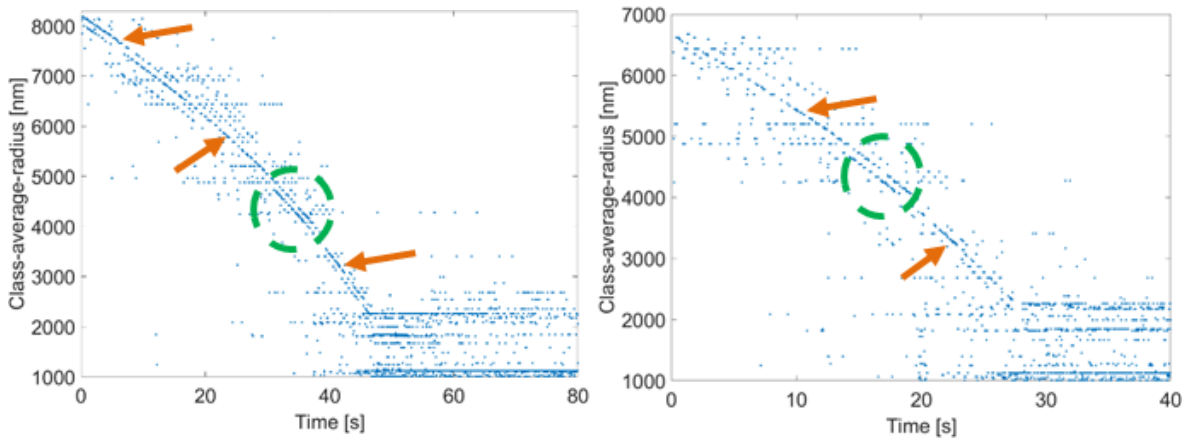


Figure 4.6: Result of classification of experimental Mie scattering patterns from two microdroplets of suspension of silica nanospheres in dipropylene glycol-water mixture. The evaporation was performed at 25±0.2ºC

Part III

4.4 Classification of size- and concentration-driven speckle changes recorded from the "*microdroplet medium*"

As presented in chapter 3, the size-controlled speckle measurements were performed by preparing two different suspensions of different concentrations. From each suspension, microdroplets of different sizes (diameter) were produced using the droplet injector. The concentration-controlled speckle measurements, on the other hand, were performed by preparing multiple concentrations of suspensions, while attempts were made to keep the droplet size similar. For each concentration, measurements were taken from two droplets, thus 1000 speckle patterns from each droplet. In order not to be confused with the nomenclature used in Part II, Drop-1 and Drop-2 are adopted here. In both cases the droplets were levitated in the linear electrodynamic trap for measurements. The droplet's shadow was measured to estimate its size and the speckle patterns were recorded for the neural network training.

4.4.1 Size-driven speckle changes from the "*microdroplet medium*"

As discussed above, two different samples were produced (15 mg/ml of Gd_2O_3 : 1% Er : 18% Yb : 0.25% Nd (ø= 212 nm) nanoparticles in DEG and 50 mg/ml of Gd_2O_3 : 1% Nd (ø= 305 nm) nanoparticles in DEG; here, the doping was of no importance). Henceforth these suspensions will be referred to as "Sample 1" and "Sample 2" respectively. Nine droplets were trapped and measured from Sample 1 while seven droplets were trapped and measured from Sample 2. The speckle patterns measured from Sample 2 are presented in Figure 4.7. For ease of reference and representation, the speckle patterns have been labeled (A - G) in Figure 4.7 and Table 4.1, where the estimated diameters have been presented for both samples. The speckle patterns recorded from Sample 1 have not been shown since they appear very similar to those presented in Figure 4.7. However, their estimated diameters have been presented in Table 4.1. Though the droplets were not trapped in order of increasing diameter, they have been arranged as such for comparison's sake.

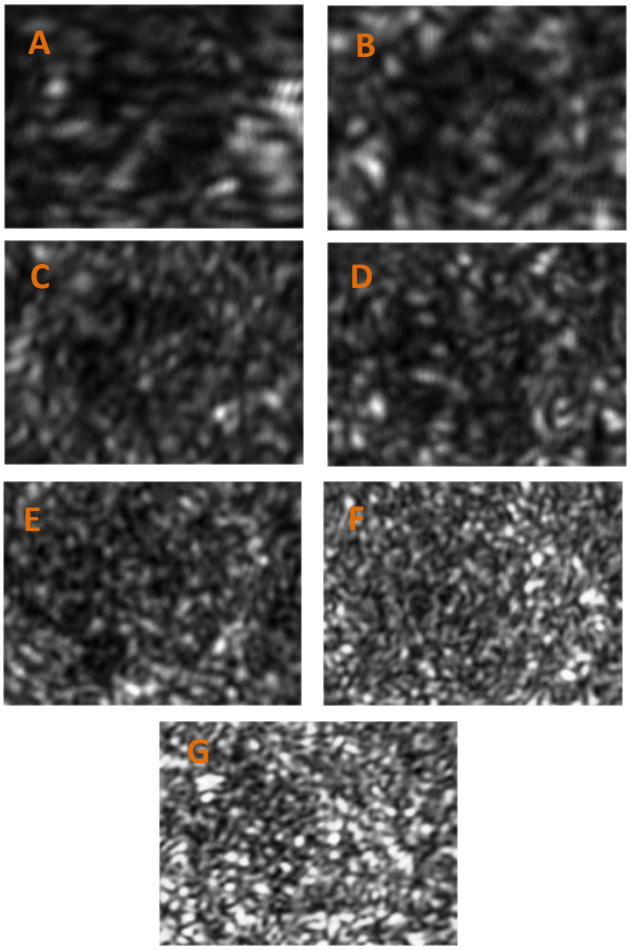


Figure 4.7: Speckle patterns (labeled A – G) recorded from seven microdroplets of Sample 2 (50 mg/ml of Gd_2O_3 : 1% Nd (ø= 305 nm)). The estimated diameters of the microdroplets have been presented in Table 4.1. The characteristic increase in number of bright regions in the speckle patterns as the droplet size increases can be seen.

In both cases, the same exposure time

(10 ms) was used to record the speckle and each image was normalized by its highest intensity value. The characteristic increase in intensity and the number of bright regions in the speckle patterns as the droplet size increases can be seen in Figure 4.7

Droplets	Diameter (µm)		
	Sample 1	Sample 2 – Label	
1	56.2	35.9	A
2	76.2	42.6	B
3	92. 8	61.6	C
4	101.4	62.5	D
5	103.1	75.5	E
6	111.1	95.9	F
7	112.6	96.8	G
8	116.4		
9	124.5		

Table 4.1: Droplets labels and estimated diameters corresponding to the speckle patterns presented in Figure 4.7

The neural network was trained separately on each sample – thus 1000 images from each droplet resulting in a total of 9000 and 7000 images for Sample 1 and Sample 2 respectively. In both cases, the data was divided into "Training", "Validation" and "Test" sets in proportions of 8:1:1, respectively for network training. The independent set could not be composed here, which is of course a severe drawback, because of the lack of guarantee that the droplets trapped would have equal diameters as the diameters of the droplets in the training data. The result of classification for both samples are presented in Figure 4.8. The "Validation" and "Test" sets accuracies obtained for Sample 1 were respectively 96.44 % and 97.5 % while the accuracies for Sample 2 were respectively 96.29 % and 97.43 % for "Validation" and "Test" sets. There was no sense in classifying Sample 2 with the network trained on Sample 1, since the samples had different concentrations and nano-particle sizes. To check the generalization capabilities of the network, many more droplets of the same suspension (concentration) must be recorded.

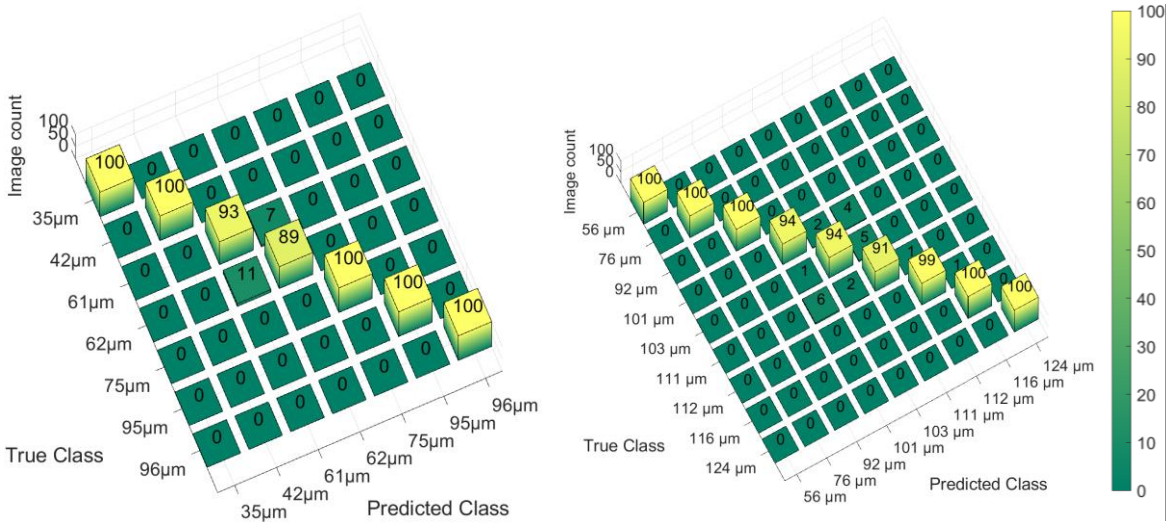


Figure 4. 8: Classification of speckle patterns recorded from microdroplets of different sizes produced from a suspension of 50 mg/ml of Gd_2O_3 : 1% Nd (ø= 305 nm) nanoparticles in DEG (left panel) and 15 mg/ml of Gd_2O_3 : 1% Er : 18% Yb : 0.25% Nd (ø= 212 nm) nanoparticles in DEG (right panel).

4.4.2 Concentration-driven speckle changes from the "*microdroplet medium*"

Five different suspensions were produced for these measurements (see Table 4.2). Technically, it was expected that equal droplet sizes would be produced from each concentration. So that the speckle changes can be encoded in only the change in concentration. However, as

discussed in section 3.3.2, several factors hindered the injection of exactly equal sizes of the droplets. Nonetheless, efforts were made to inject equal sizes of the droplets. In Table 4.2, the estimated diameters for Drop-1 and Drop-2 as well as their average diameters for each concentration have been presented.

Concentration (mg/ml)	Droplet diameter (µm)		
	Drop-1	Drop-2	Average
5	103. 8	104. 8	104.3
10	101.2	89. 8	95.5
20	116.5	93.2	104.9
30	83.3	109.4	96.3
50	84.6	110.4	97.5

Table 4.2: Estimated diameters of microdroplets produced from different concentrations of Gd_2O_3 : 1% Nd (ø= 305 nm) nanoparticles in DEG.

As can be seen in the table, there are slight differences between diameters of Drop-1 and Drop-2 and between droplets of different concentrations. The differences, in some cases, are less than 1 µm and in other cases higher. For example, the difference in average diameter between 5 and 20 mg/ml and 10 and 30 mg/ml are respectively 0.6 and 0.8 µm while 30 and 50 mg/ml and 10 and 20 mg/ml is respectively 1.2 and 9.4 µm.

Since the parameter that was varied to cause the change in speckle pattern is the concentration, it is expected that it would manifest as increase in intensities for higher concentrations. On the other hand, the uncertainty of the number of particles in each microdroplet upon ejection from the droplet injector and the uncertainty of the number of such particles in the viewing volume are also expected to influence this phenomenon. In Figure 4.9, the speckle patterns recorded from each droplet are presented. The patterns are presented from left to right for increasing concentration, top panel, Drop-1 and bottom panel, Drop-2 for each concentration. Among all the patterns presented in Figure 4.9, the droplets recorded from 50 mg/ml produced the highest intensity as expected. On the other hand, the droplets produced from the 5 mg/ml suspension produced weak intensities (also as expected), resulting in low signal-to-noise ratio and a manifestation of artifacts from the optical system.

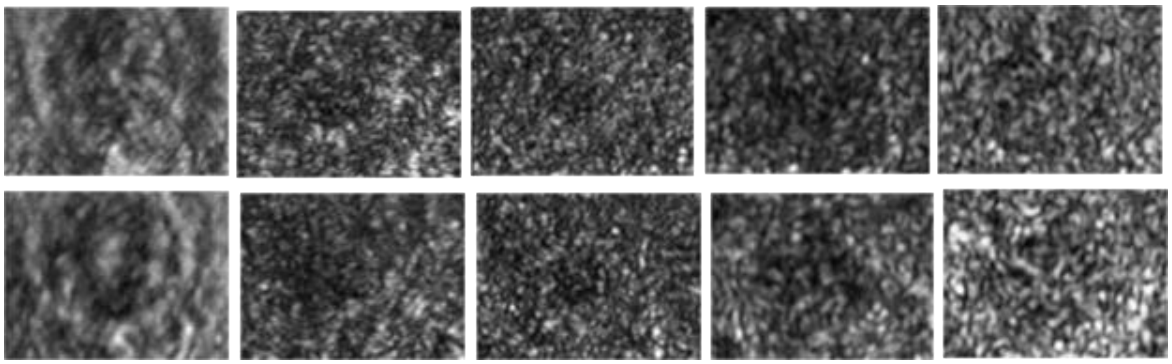


Figure 4.9: Speckle patterns recorded from microdroplets of different concentrations of suspensions. From left to right, increasing concentration, top panel, Drop-1 for each concentration and bottom panel, Drop-2 for each concentration.

Figure 4.10 represents the classification of speckle patterns recorded from the different concentrations of Gd_2O_3 : 1% Nd (ø= 305 nm) nanoparticles in DEG. The data was composed by combining all the speckle patterns from one Drop-1 and half from Drop-2 – thus 1500 in total for each concentration and 7500 for the whole sample set. This data was then divided into

"Training", "Validation" and "Test" sets as discussed above. The remaining 500 speckle patterns served as the "Independent" set. Accuracies of 99.69%, 96.00% and 92.04% were achieved for "Validation", "Test" and "Independent" sets respectively. The 5 mg/ml case should be excluded, since it may well be expected that the network learned the artifacts present in the images. Considering the remaining cases, though the network trained very well, the conclusion that the concentration can be reliably recognized cannot be safely drawn at this point – the training data was too sparse versus the diameter variability, or otherwise the diameter variability was still too large. Further experiments are still required.

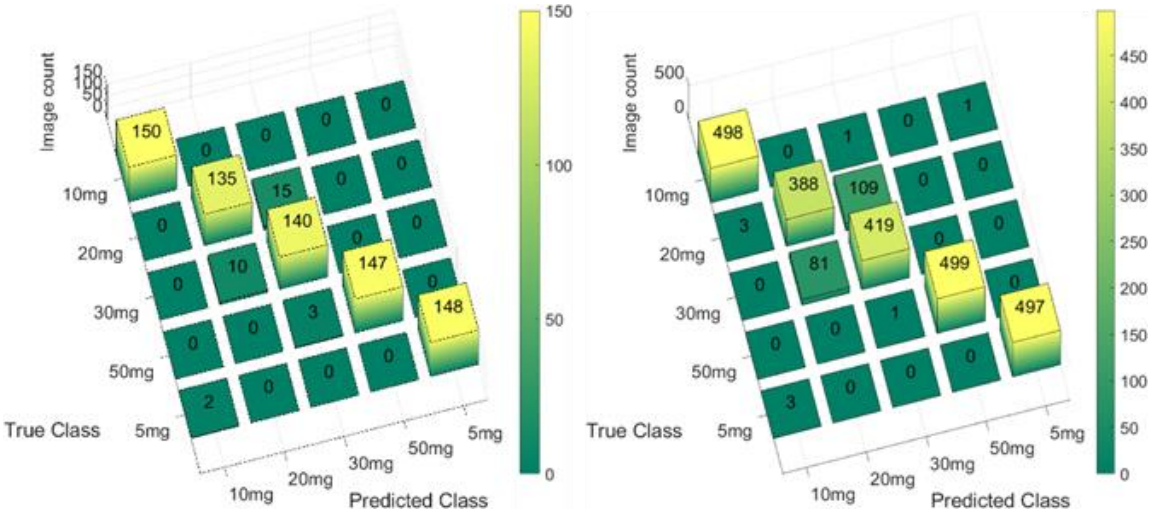


Figure 4.10: Classification of speckle patterns recorded from microdroplets of suspensions of different concentrations (in mg/ml) of Gd_2O_3 : 1% Nd (ø= 305 nm) nanoparticles in DEG. Left panel, result of classification of "Test" set, right panel, results of classification of "Independent" set.

Nonetheless, the general ability of the network to train for both size- and concentration-controlled speckle measurements from the microdroplet's media seems to confirm the very promising future applications of microdroplets of suspensions as micro-cuvettes for particle characterization (in terms of type, inclusion size and/or concentration). Quite in line with what has already been demonstrated by [107] who performed chemical reactions of microdroplets of different substances in a branched quadrupole trap, as already discussed in chapter 2. It must, however, be emphasized that for such future applications of this technique with neural networks, larger data sets (with chosen/desired parameters) are required for training the network. As can be inferred from the results presented above, the size variation of droplets in the concentration-controlled measurements and the inability to perform size-tailored measurements are still yet to be circumvented. Hence, the results of the measurements presented above should be seen as proof-of-principle.

4.5 Comparison between the "bulk medium" and "microdroplet medium"

Despite the fact that the "*bulk medium*" consisted of milk as a colloidal suspension and the *"microdroplet medium"* consisted of nano-particles, several aspects of the two media may be compared.

Firstly, the 0.05 mm-thickness of the cuvette volume together with the 1.7 mm diameter of the laser beam result in (an idealized) cylindrical scattering volume in the "*bulk medium*". This scattering volume of the suspension is significantly larger compared with the volume of the microdroplets.

In the cuvette, the laser interacts with both the freely moving particles in the volume of the suspension and (somewhat restricted) particles of the milk which are in contact with the substrates (on both sides). On the other hand, the droplet is not in contact with any solid surface. In the volume of the microdroplet, the particles are moving freely, while a specific restriction may occur when the particles emerge and get stacked on the surface.

Furthermore, in the "*bulk medium*" a near forward (26.9^{o} from the exit beam) transmitted speckle patterns were measured. This configuration ensures that the scattering is strong, while (when single scattering is considered) it depends more strongly on the scatterers size than on their refractive index (contrast). On the other hand, scattering at 90^{o} angle was measured from the microdroplets. Scattering at a right angle is generally more sensitive to refractive index of scatterers, however it must be kept in mind that the field inside a droplet – a spherical resonator – and thus scattered on the suspended particles, cannot be considered as directional. We take, however, great advantage of resonance properties of the system (droplet + particles in suspended phase), which greatly increases its sensitivity to minute changes. Though weaker in intensity due to droplet size and thus the number of scatterers as compared to the "*bulk medium"*, the results show that even the small changes in droplet diameter and suspension properties can be detected and measured.

Chapter 5
Summary, Conclusions and Recommendations

5.1 Chapter overview

In this chapter, a summary of the study and key findings will be presented alongside some recommendations for further studies and applications. It is expected that these conclusions and recommendations will be useful in achieving the ultimate goal of the larger project. Finally, the declarations of contribution to each publication reproduced in Chapter 4, signed by each co-author, will be presented in the Appendix.

5.2 Summary and Conclusions

As outlined in the problem statement of this study, (see chapter 1), several aspects of the ultimate goal of the project have been achieved. In one aspect, speckle measurements were combined with convolutional neural networks for the recognition/classification of the parameters of suspensions in a "*bulk medium*".

In the "*bulk medium*", 10 μL of milk (which is a complex realistic suspension) samples of different fat contents were loaded into a thin cuvette and a much smaller scattering volume (0.05 mm-thick by 1.7 mm diameter) of the milk was illuminated with a laser. Speckle patterns were generated and recorded using four different exposure-time protocols. A 35-layer convolutional neural network was trained in a classification task. It was found that the network trains better, produces higher accuracies and is very stable when the speckles were recorded with shorter exposure times (but the same within one class) and the intensity histograms were kept similar for all samples such that the most probable intensity is as close to zero as possible. Though the network also produced high accuracies on the classification of the test sets for longer exposure times (but the same within one class) and varying exposure times within one class, training robustness and generalisation performance on the independent sets varied across protocols. Among them, one methodologically sound protocol was identified as optimal.

In the other aspect of the measurements, "*microdroplet medium*", both Mie theory and the speckle phenomenon were combined with convolutional neural networks to recognize/classify the parameters of pure liquids, liquid-mixtures and suspensions. As outlined already, Mie theory and its experimental methods have long been used to measure accurately the size of various spherical particles and tracking of evaporation rates of microdroplets (in general, particle characterization) by many authors. The results presented in this study show how convolutional neural networks (upgraded to 41 layers) were trained (perhaps, the first time in a classification task) to recognize Mie scattering patterns recorded from evaporating microdroplets of pure liquids, liquid-mixtures and suspensions leading to the tracking of their evaporation rate.

A wider radii range (1 – 30 μm) was divider into classes of smaller radii ranges and theoretical Mie scattering patterns were generated for network training. The trained network was then used to classify similar experimental scattering patterns sequentially. For microdroplets produced from pure liquids, it was found that the network was able to produce high classifications of the experimental data into their appropriate classes when the radii range was divided

into class intervals of 10 nm. So that the error was estimated as ± 5 nm from the class average radius. With this class interval and accuracy, the evaporation rates of microdroplets of pure liquids were tracked and smooth evaporation curves for each droplet could be inferred with reasonable accuracy.

The results obtained from the microdroplets of liquid-mixtures and suspensions were rather plagued with the effects of varying refractive index and distortions of the Mie scattering patterns by the nano-particles in the microdroplets. Though the classification revealed the trends of the evaporation curves, multiple "branches" of the curves were obtained, corresponding to different possible scenarios of evolution.

In the case of speckle measurements from the microdroplets of suspensions, the diameters of the microdroplets and the concentrations of the suspensions were encoded in the speckle pattern. The study, though, should be seen as a proof-of-principle, the results reveal the significant potential of the technique in particle characterization.

5.3 Recommendations

This study did not only emphasize the potential of combining optical measurement with the fast and accurate processing of data by neural networks (as an optical-numerical system) but also produced interesting results worth further investigations and application. However, before such endeavours the following recommendations may be considered first:

(i) The results obtained from the classification of Mie scattering patterns recorded from microdroplets of suspensions and liquid-mixtures require optimization with regards to finding/handling the effective refractive index. A single value, either corresponding to the main component or found by fitting – using a few mean scattering vectors, is not sufficient. It is recommended that a gradual variation of the refractive index should be accounted for somehow. It may be achieved in two ways: (i) varying/changing the refractive index of the main component gradually, training the network on each value and classifying the experimental data until a smooth evaporation curve is obtained (though the training would be very time-consuming) and (ii) varying the refractive index between radii ranges, as was done here (but with the same refractive index along the evaporation curve). In this approach, a single network may be trained on each radius range (or classes with varying refractive indices) or series of networks for given radii ranges (or even refractive-index-oriented networks). It must, however, be mentioned that this approach would require an accurate determination of the change in refractive index withing such chosen radii or classes from experimental measurements.

(ii) The two optical systems designed for the separate experimental measurements of Mie scattering and speckle patterns can be combined into one experimental setup. This can be achieved by recording the Mie scattering around the 90^{o} angle (as discussed in the study) while the speckle pattern can be recorded around the 270^{o} angle, so that both can be recorded simultaneously. With such a setup, the size variation of the evaporating microdroplet can be, in many cases, more accurately

measured from the Mie scattering patterns, providing a better input for network training on concentration variation and speckle measurements during evaporation.

(iii) Finally, large data sets are required for training the convolutional neural network on experimental data. For example, trapping and recording Mie scattering patterns from nearly a million (or more) evaporating microdroplets and using standard Mie calculations to accurately retrieve their sizes and refractive indices will provide a well-diversified and accurately labelled data. Creating such data sets, though, require both human and computer resources, could possibly serve as a reference data set for the light scattering community and the scientific community at large.

5.4 Appendix

ANALYSIS RESULT

	Name	Type	Activations	Learnable Properties	States
1	input 221×501×1 images	Image Input	221(S) × 501(S) × 1(C) × 1(B)	-	-
2	conv1 64 3×3×1 convolutions with stride [1 1] and padding [0 0 0 0]	2-D Convolution	219(S) × 499(S) × 64(C) × 1(B)	Weights 3 × 3 × 1 × 64 Bias 1 × 1 × 64	-
3	BN1 Batch normalization with 64 channels	Batch Normalization	219(S) × 499(S) × 64(C) × 1(B)	Offset 1 × 1 × 64 Scale 1 × 1 × 64	TrainedMean 1 × 1 × 64 TrainedVariance 1 × 1 × 64
4	relu1 ReLU	ReLU	219(S) × 499(S) × 64(C) × 1(B)	-	-
5	MP1 3×3 max pooling with stride [2 2] and padding [0 0 0 0]	2-D Max Pooling	109(S) × 249(S) × 64(C) × 1(B)	-	-
6	conv2 64 3×3×64 convolutions with stride [2 2] and padding [1 1 1 1]	2-D Convolution	55(S) × 125(S) × 64(C) × 1(B)	Weights 3 × 3 × 64 × 64 Bias 1 × 1 × 64	-
7	BN2 Batch normalization with 64 channels	Batch Normalization	55(S) × 125(S) × 64(C) × 1(B)	Offset 1 × 1 × 64 Scale 1 × 1 × 64	TrainedMean 1 × 1 × 64 TrainedVariance 1 × 1 × 64
8	relu2 ReLU	ReLU	55(S) × 125(S) × 64(C) × 1(B)	-	-
9	conv3 64 3×3×64 convolutions with stride [1 1] and padding [1 1 1 1]	2-D Convolution	55(S) × 125(S) × 64(C) × 1(B)	Weights 3 × 3 × 64 × 64 Bias 1 × 1 × 64	-
10	skipConv1 64 1×1×64 convolutions with stride [2 2] and padding [0 0 0 0]	2-D Convolution	55(S) × 125(S) × 64(C) × 1(B)	Weights 1 × 1 × 64 × 64 Bias 1 × 1 × 64	-
11	add1 Element-wise addition of 2 inputs	Addition	55(S) × 125(S) × 64(C) × 1(B)	-	-
12	BN3 Batch normalization with 64 channels	Batch Normalization	55(S) × 125(S) × 64(C) × 1(B)	Offset 1 × 1 × 64 Scale 1 × 1 × 64	TrainedMean 1 × 1 × 64 TrainedVariance 1 × 1 × 64
13	relu3 ReLU	ReLU	55(S) × 125(S) × 64(C) × 1(B)	-	-
14	MP3 3×3 max pooling with stride [2 2] and padding [0 0 0 0]	2-D Max Pooling	27(S) × 62(S) × 64(C) × 1(B)	-	-
15	conv4 64 3×3×64 convolutions with stride [1 1] and padding [1 1 1 1]	2-D Convolution	27(S) × 62(S) × 64(C) × 1(B)	Weights 3 × 3 × 64 × 64 Bias 1 × 1 × 64	-
16	BN4 Batch normalization with 64 channels	Batch Normalization	27(S) × 62(S) × 64(C) × 1(B)	Offset 1 × 1 × 64 Scale 1 × 1 × 64	TrainedMean 1 × 1 × 64 TrainedVariance 1 × 1 × 64
17	relu4 ReLU	ReLU	27(S) × 62(S) × 64(C) × 1(B)	-	-
18	conv5 64 3×3×64 convolutions with stride [2 2] and padding [1 1 1 1]	2-D Convolution	14(S) × 31(S) × 64(C) × 1(B)	Weights 3 × 3 × 64 × 64 Bias 1 × 1 × 64	-
19	skipConv2 64 1×1×64 convolutions with stride [2 2] and padding [0 0 0 0]	2-D Convolution	14(S) × 31(S) × 64(C) × 1(B)	Weights 1 × 1 × 64 × 64 Bias 1 × 1 × 64	-
20	add2 Element-wise addition of 2 inputs	Addition	14(S) × 31(S) × 64(C) × 1(B)	-	-
21	BN5 Batch normalization with 64 channels	Batch Normalization	14(S) × 31(S) × 64(C) × 1(B)	Offset 1 × 1 × 64 Scale 1 × 1 × 64	TrainedMean 1 × 1 × 64 TrainedVariance 1 × 1 × 64

Table 5.1: Detailed analysis of Stage 2_2 network provided by MATLAB's deep network analyser. The parameters of each layer from input (1) to BN5 (21) can be seen, while the continuation (22 to 41) is provided on page 84.

22	relu5 ReLU	ReLU	14(S) × 31(S) × 64(C) × 1(B)	-	-
23	MP5 3×3 max pooling with stride [1 1] and padding [0 0 0 0]	2-D Max Pooling	12(S) × 29(S) × 64(C) × 1(B)	-	-
24	conv6A 128 3×3×64 convolutions with stride [1 1] and padding [1 1 1 1]	2-D Convolution	12(S) × 29(S) × 128(C) × 1(B)	Weights 3 × 3 × 64 × 128 Bias 1 × 1 × 128	-
25	BN6A Batch normalization with 128 channels	Batch Normalization	12(S) × 29(S) × 128(C) × 1(B)	Offset 1 × 1 × 128 Scale 1 × 1 × 128	TrainedMean 1 × 1 × 128 TrainedVariance 1 × 1 × 128
26	relu6A ReLU	ReLU	12(S) × 29(S) × 128(C) × 1(B)	-	-
27	MP6A 3×3 max pooling with stride [1 1] and padding [0 0 0 0]	2-D Max Pooling	10(S) × 27(S) × 128(C) × 1(B)	-	-
28	conv7A 256 3×3×128 convolutions with stride [2 2] and padding [1 1 1 1]	2-D Convolution	5(S) × 14(S) × 256(C) × 1(B)	Weights 3 × 3 × 128 × 256 Bias 1 × 1 × 256	-
29	BN7A Batch normalization with 256 channels	Batch Normalization	5(S) × 14(S) × 256(C) × 1(B)	Offset 1 × 1 × 256 Scale 1 × 1 × 256	TrainedMean 1 × 1 × 256 TrainedVariance 1 × 1 × 256
30	relu7A ReLU	ReLU	5(S) × 14(S) × 256(C) × 1(B)	-	-
31	conv6B 256 3×3×64 convolutions with stride [1 1] and padding [1 1 1 1]	2-D Convolution	12(S) × 29(S) × 256(C) × 1(B)	Weights 3 × 3 × 64 × 256 Bias 1 × 1 × 256	-
32	BN6B Batch normalization with 256 channels	Batch Normalization	12(S) × 29(S) × 256(C) × 1(B)	Offset 1 × 1 × 256 Scale 1 × 1 × 256	TrainedMean 1 × 1 × 256 TrainedVariance 1 × 1 × 256
33	relu6B ReLU	ReLU	12(S) × 29(S) × 256(C) × 1(B)	-	-
34	MP6B 3×3 max pooling with stride [1 1] and padding [0 0 0 0]	2-D Max Pooling	10(S) × 27(S) × 256(C) × 1(B)	-	-
35	conv7B 382 3×3×256 convolutions with stride [2 2] and padding [1 1 1 1]	2-D Convolution	5(S) × 14(S) × 382(C) × 1(B)	Weights 3 × 3 × 256 × 382 Bias 1 × 1 × 382	-
36	BN7B Batch normalization with 382 channels	Batch Normalization	5(S) × 14(S) × 382(C) × 1(B)	Offset 1 × 1 × 382 Scale 1 × 1 × 382	TrainedMean 1 × 1 × 382 TrainedVariance 1 × 1 × 382
37	relu7B ReLU	ReLU	5(S) × 14(S) × 382(C) × 1(B)	-	-
38	concat_1 Depth concatenation of 2 inputs	Depth concatenation	5(S) × 14(S) × 638(C) × 1(B)	-	-
39	fc3 1401 fully connected layer	Fully Connected	1(S) × 1(S) × 1401(C) × 1(B)	Weights 1401 × 44660 Bias 1401 × 1	-
40	softmax softmax	Softmax	1(S) × 1(S) × 1401(C) × 1(B)	-	-
41	classif crossentropyex with 'Class1' and 1400 other classes	Classification Output	1(S) × 1(S) × 1401(C) × 1(B)	-	-

A continuation of Table 5.1

Declaration of contributions by co-authors to the publications

MSc. Kwasi Nyandey
Institute of Physics, Polish Academy of Sciences
al. Lotników 32/46, 02-668, Warsaw, Poland
E-mail: nyandey@ifpan.edu.pl/kwasi.nyandey@ucc.edu.gh

STATEMENT

I declare that I am a co-author of the publication:

> K. Nyandey and D. Jakubczyk, "*Combining transmission speckle photography and convolutional neural network for determination of fat content in cow milk: an exercise in classification of parameters of a complex suspension*," Eur. Phys. J. Plus, 139,123, Feb. 2024.

My contributions included writing – original draft, software, methodology, investigation, data curation and review & editing,

Warsaw, 02.06.2025



dr. hab. eng. Daniel Jakubczyk
Head of the Group of Optical Characterisation of Micro-and Nanoobjects
Institute of Physics, Polish Academy of Sciences
al. Lotników 32/46, 02-668 Warsaw, Poland
e-mail: jakub@ifpan.edu.pl

STATEMENT

I declare that I am a co-author of the publication:

> K. Nyandey and D. Jakubczyk, "*Combining transmission speckle photography and convolutional neural network for determination of fat content in cow milk: an exercise in classification of parameters of a complex suspension*," Eur. Phys. J. Plus, 139, 123, Feb. 2024.

My contributions included review & editing, data visualization & validation, project supervision & administration and funding acquisition.

Warsaw, 02.06.2025



Podpisany certyfikatem wystawionym dla Daniel Jakubczyk (Certyfikat kwalifikowany). Utworzony w dniu: 2025-06-02 14:54:49 +0200

MSc. Kwasi Nyandey
Institute of Physics, Polish Academy of Sciences
al. Lotników 32/46, 02-668, Warsaw, Poland
E-mail: nyandey@ifpan.edu.pl/kwasi.nyandey@ucc.edu.gh

STATEMENT

I declare that I am a co-author of the publication:

> K. Nyandey, G. Derkachov, and D. Jakubczyk, "*A convolutional neural network technique for online tracking of the radius evolution of levitating evaporating microdroplets of pure liquids, liquid mixtures and suspensions*," *J. Quant. Spectrosc. Radiat. Transf.*, 344, 109533, May 2025.

My contributions included writing – original draft, software, methodology, investigation, data curation and review & editing,

Warsaw, 02.06.2025



Dr. Gennadiy Derkachov
Institute of Physics, Polish Academy of Sciences
al. Lotników 32/46, 02-668, Warsaw, Poland
E-mail: derkaczg@ifpan.edu.pl

STATEMENT

I declare that I am a co-author of the publication:

> K. Nyandey, G. Derkachov, and D. Jakubczyk, "*A convolutional neural network technique for online tracking of the radius evolution of levitating evaporating microdroplets of pure liquids, liquid mixtures and suspensions*," *J. Quant. Spectrosc. Radiat. Transf.*, 344, 109533, May 2025..

My contributions included review & editing, software resources and data curation

Warsaw, 03.06.2025

G. Derkachov

dr. hab. eng. Daniel Jakubczyk
Head of the Group of Optical Characterisation of Micro-and Nanoobjects
Institute of Physics, Polish Academy of Sciences
al. Lotników 32/46, 02-668 Warsaw, Poland
e-mail: jakub@ifpan.edu.pl

STATEMENT

I declare that I am a co-author of the publication:

> K. Nyandey, G. Derkachov, and D. Jakubczyk, "*A convolutional neural network technique for online tracking of the radius evolution of levitating evaporating microdroplets of pure liquids, liquid mixtures and suspensions*," *J. Quant. Spectrosc. Radiat. Transf.*, 344, 109533, May 2025.

My contributions included review & editing, data visualization & validation, project supervision & administration and funding acquisition.

Warsaw, 02.06.2025



Podpisany certyfikatem wystawionym dla Daniel Jakubczyk (Certyfikat kwalifikowany). Utworzony w dniu: 2025-06-02 14:54:49 +0200

5.5 References

[1] N. A. Logan, "Survey of Some Early Studies of the Scattering of Plane Waves by a Sphere," *Proc. IEEE*, vol. 53, no. 8, pp. 773–785, 1965, doi: 10.1109/PROC.1965.4055.

[2] G. Gouesbet and G. Gréhan, *Generalized Lorenz-Mie Theories*, 3rd ed. Springer Cham, 2023. doi: 10.1007/978-3-031-25949-4.

[3] T. Wriedt, "A Review of Elastic Light Scattering Theories," *Part. Part. Syst. Charact.*, vol. 15, no. 2, pp. 67–74, Apr. 1998, doi: 10.1002/(SICI)1521-4117(199804)15:2<67::AID-PPSC67>3.0.CO;2-F.

[4] C. F. . Bohren and D. R. . Huffman, *Absorption and scattering of light by small particles*. Wiley, 1998.

[5] G. Mie, "Beiträge zur Optik trüber Medien, speziell kolloidaler Metallösungen," *Ann. Phys.*, vol. 330, no. 3, pp. 377–445, 1908, doi: 10.1002/andp.19083300302.

[6] R. Xu, *Particle Characterization: Light Scattering Methods*, Vol. 13. Springer Science & Business Media, 2001.

[7] R. Xu, "Light scattering: A review of particle characterization applications," Feb. 01, 2015, *Elsevier B.V.* doi: 10.1016/j.partic.2014.05.002.

[8] G. Mie, "Contributions to the optics of turbid media, particularly of colloidal metal solutions," 1908. doi: 10.1002/andp.19083300302.

[9] H. van de Hulst, "Light Scattering by Small Particles," 1981.

[10] T. Wriedt and W. Hergert, *The Mie Theory Basics and Applications*. [Online]. Available: http://www.springer.com/series/624

[11] M. Nieto-Vesperinas, "Fundamentals of Mie scattering," in *Dielectric Metamaterials*, Elsevier, 2020, pp. 39–72. doi: 10.1016/B978-0-08-102403-4.00007-4.

[12] "ScattPort Home." Accessed: Apr. 29, 2025. [Online]. Available: https://scattport.org/index.php

[13] "Mie Theory 1908-2008." Accessed: Apr. 29, 2025. [Online]. Available: https://scattport.org/index.php/mie-theory-1908-2008

[14] D. K. Hahn and S. R. Aragón, "MIE scattering from anisotropic thick spherical shells," *J. Chem. Phys.*, vol. 101, no. 10, pp. 8409–8417, 1994, doi: 10.1063/1.468103.

[15] T. Kaiser and G. Schweiger, "Stable algorithm for the computation of Mie coefficients for scattered and transmitted fields of a coated sphere," *Comput. Phys.*, vol. 7, no. 6, pp. 682–686, Nov. 1993, doi: 10.1063/1.168475.

[16] M. Kerker, P. Scheiner, and D. D. Cooke, "The range of validity of the Rayleigh and Thomson limits for Lorenz-Mie scattering," *J. Opt. Soc. Am.*, vol. 68, no. 1, p. 135, 1978, doi: 10.1364/josa.68.000135.

[17] M. Kerker, D. S. Wang, and C. L. Giles, "Electromagnetic Scattering By Magnetic Spheres.," *J. Opt. Soc. Am.*, vol. 73, no. 6, pp. 765–767, 1983, doi: 10.1364/JOSA.73.000765.

[18] A. L. Aden and M. Kerker, "Scattering of electromagnetic waves from two concentric spheres," *J. Appl. Phys.*, vol. 22, no. 10, pp. 1242–1246, 1951, doi: 10.1063/1.1699834.

[19] G. Gouesbet, "Generalized Lorenz-Mie Theory and Applications," *Part. Part. Svst. Charact. I1*, vol. 11, no. 1, pp. 22–34, 1994, doi: 10.1002/ppsc.19940110105.

[20] J. A. Lock, "Contribution of high-order rainbows to the scattering of a Gaussian laser beam by a spherical particle," *J. Opt. Soc. Am. A*, vol. 10, no. 4, 1993, doi: 10.1364/JOSAA.10.000693.

[21] G. Gouesbet and G. Gréhan, "Laser-based optical measurement techniques of discrete particles: A review [invited keynote]," *Int. J. Multiph. Flow*, vol. 72, pp. 288–297, Jun. 2015, doi: 10.1016/j.ijmultiphaseflow.2014.07.001.

[22] T. Wriedt, “Light scattering theories and computer codes,” *J. Quant. Spectrosc. Radiat. Transf.*, vol. 110, no. 11, pp. 833–843, Jul. 2009, doi: 10.1016/j.jqsrt.2009.02.023.
[23] “t-matrix.de.” Accessed: Apr. 30, 2025. [Online]. Available: https://www4.t-matrix.de/
[24] T. Wriedt, “Mie theory 1908, on the mobile phone 2008,” *J. Quant. Spectrosc. Radiat. Transf.*, vol. 109, no. 8, pp. 1543–1548, May 2008, doi: 10.1016/j.jqsrt.2008.01.009.
[25] R. J. Zhu, J. Wang, and G. F. Jin, “Mie scattering calculation by FDTD employing a modified Debye model for Gold material,” *Optik (Stuttg).*, vol. 116, no. 9, pp. 419–422, 2005, doi: 10.1016/j.ijleo.2005.01.035.
[26] T. Grosges, A. Vial, and D. Barchiesi, “Models of near-field spectroscopic studies: comparison between Finit-Element and Finit-Differnce methods,” *Opt. Express*, vol. 13, no. 21, 2005.
[27] P. Yang and K. N. Liou, “Finite-difference time domain method for light scattering by small ice crystals in three-dimensional space,” *J. Opt. Soc. Am. A*, vol. 13, no. 10, 1996, doi: 10.1364/JOSAA.13.002072.
[28] N. Asadova *et al.*, “T-matrix representation of optical scattering response: Suggestion for a data format,” *J. Quant. Spectrosc. Radiat. Transf.*, vol. 333, p. 109310, Mar. 2025, doi: 10.1016/j.jqsrt.2024.109310.
[29] D. W. Mackowski and M. I. Mishchenko, “Calculation of the T matrix and the scattering matrix for ensembles of spheres,” *J. Opt. Soc. Am. A*, vol. 13, no. 11, 1996, doi: 10.1364/JOSAA.13.002266.
[30] G. Gouesbet, “T-matrix formulation and generalized Lorenz-Mie theories in spherical coordinates,” *Opt. Commun.*, vol. 283, no. 4, pp. 517–521, Feb. 2010, doi: 10.1016/j.optcom.2009.10.092.
[31] M. I. Mishchenko, L. D. Travis, and D. W. Mackowski, “T-Matrix Computations of Light Scattering by Non-Spherical Particles: A Review,” *J. Quant. Spectrosc. Radial. Transf.*, vol. 55, no. 5, pp. 535–515, 1996, doi: 10.1016/0022-4073(96)00002-7.
[32] A. A. L. Michael I. Mishchenko, Larry D. Travis, *Scattering, Absorption, and Emission of Light by Small Particles*. Cambridge University Press, 2004.
[33] M. I. Mishchenko, J. W. Hovenier, and L. D. Travis, *Light Scattering by Nonspherical Particles Theory, Measurements, and Applications*. Academic Press, 2000.
[34] E. Hecht, *Optics*, 4th ed. Addison Wesley, 2002. doi: 10.1201/9781003525899-5.
[35] P. C. Waterman, “Matrix Formulation of Electromagnetic Scattering,” *Proc. IEEE*, vol. 53, no. 8, pp. 805–812, 1965, doi: 10.1109/PROC.1965.4058.
[36] J. A. Morrison and M.-J. Cross, “Scattering of a Plane Electromagnetic Wave by Axisymmetric Raindrops,” *Bell Syst. Tech. J.*, vol. 53, pp. 955–1019, 1974.
[37] W.-K. Chen, Ed., *The Electrical Engineering Handbook*. Elsevier, 2004.
[38] C. M. Furse, S. P. Mathur, and O. P. Gandhi, “Improvements to the finite-difference time-domain method for calculating the radar cross section of a perfectly conducting target,” *IEEE Trans. Microw. Theory Tech.*, vol. 38, no. 7, pp. 919–927, Jul. 1990, doi: 10.1109/22.55785.
[39] Kane Yee, “Numerical solution of initial boundary value problems involving maxwell’s equations in isotropic media,” *IEEE Trans. Antennas Propag.*, vol. 14, no. 3, pp. 302–307, May 1966, doi: 10.1109/TAP.1966.1138693.
[40] A. Ludwig, “The generalized multipole technique,” 1991.
[41] J. H. Bruning and Y. T. Lo, “Multiple Scattering of EM Waves by Spheres Part I—Multipole Expansion and Ray-Optical Solutions,” *IEEE Trans. Antennas Propag.*, vol. 19, no. 3, pp. 378–390, 1971, doi: 10.1109/TAP.1971.1139944.
[42] M. Woźniak *et al.*, “Application of a linear electrodynamic quadrupole trap for production of nanoparticle aggregates from drying microdroplets of colloidal

suspension," *J. Instrum.*, vol. 14, no. 12, 2019, doi: 10.1088/1748-0221/14/12/P12007.
[43] G. Gouesbet and G. Gréhan, "Generalized Lorenz-Mie theory for a sphere with an eccentrically located spherical inclusion," *J. Mod. Opt.*, vol. 47, no. 5, pp. 821–837, 2000, doi: 10.1080/09500340008235093.
[44] J. W. Goodman, *Laser Speckle and Related Phenomena*, vol. 9. Berlin: Springer, 1975.
[45] P. Lehmann, "Surface-roughness measurement based on the intensity correlation function of scattered light under speckle-pattern illumination," *Appl. Opt.*, vol. 38, no. 7, p. 1144, Mar. 1999, doi: 10.1364/AO.38.001144.
[46] K. . Hinsch, T. Fricke-Begemann, G. Gülker, and K. Wolff, "Speckle correlation for the analysis of random processes at rough surfaces," *Opt. Lasers Eng.*, vol. 33, no. 2, pp. 87–105, Feb. 2000, doi: 10.1016/S0143-8166(00)00035-X.
[47] J. W. Goodman, *Statistical Optics*. John Wiley & Sons, Inc, 2000.
[48] J. W. Goodman, "Some fundamental properties of speckle*," *J. Opt. Soc. Am.*, vol. 66, no. 11, p. 1145, 1976, doi: 10.1364/josa.66.001145.
[49] Lord Rayleigh, " XII. On the resultant of a large number of vibrations of the same pitch and of arbitrary phase ," *London, Edinburgh, Dublin Philos. Mag. J. Sci.*, vol. 10, no. 60, pp. 73–78, 1880, doi: 10.1080/14786448008626893.
[50] Lord Rayleigh, "On the Problem of Random Vibrations, and of Random Fligts in one, twe, or three Dimensions," *Philos. Mag. J. Sci.*, vol. x, no. 220, 1919.
[51] L. I. Goldfischer, "Autocorrelation Function and Power Spectral Density of Laser-Produced Speckle Patterns," *J. Opt. Soc. Am. A*, vol. 55, no. March, 1965, doi: 10.1364/JOSA.55.000247.
[52] C. Li, G. W. Kattawar, and P. Yang, "Effects of surface roughness on light scattering by small particles," *J. Quant. Spectrosc. Radiat. Transf.*, vol. 89, no. 1–4, pp. 123–131, 2004, doi: 10.1016/j.jqsrt.2004.05.016.
[53] K. Nyandey, "Investigation of the effect of induced-moisture and temperature rise on the surface dynamics of wood using electronic speckle pattern interferometry," University of Cape Coast, Cape Coast, Ghana, 2018.
[54] N. A. Fomin, *Speckle Photography for Fluid Mechanics Measurements*. Berlin Heidelberg: Springer, 1998.
[55] G. Palumbo and R. Pratesi, Eds., *Lasers and Current Optical Techniques in Biology*. The Royal Society of Chemistry, 2016.
[56] E. J. Davis, "A history of single aerosol particle levitation," *Aerosol Sci. Technol.*, vol. 26, no. 3, pp. 212–254, Jan. 1997, doi: 10.1080/02786829708965426.
[57] R. A. MILLIKAN, "A new modification of the cloud method of determining the elementary electric charge," *Philos. Mag. J. Sci.*, vol. 19, no. 110, 1910.
[58] R. A. Millikan, "The Isolation of an Ion, a Precision Measurement of its Charge and the Correction of Stokes's Law," *Phys. Rev.*, vol. XXXII, no. 4, 1911, doi: 10.1103/PhysRevSeriesI.32.349.
[59] W. Paul, "Electromagnetic traps for charged and neutral particles," *Rev. Mod. Phys.*, vol. 62, no. 3, pp. 531–540, Jul. 1990, doi: 10.1103/RevModPhys.62.531.
[60] G. Göbel, T. Wriedt, and K. Bauckhage, "Periodic drag force and particle size measurement in a double ring electrodynamic trap," *Rev. Sci. Instrum.*, vol. 68, no. 8, pp. 3046–3052, 1997, doi: 10.1063/1.1148239.
[61] C. Wang, Y. Le Pan, and G. Videen, "Optical trapping and laser-spectroscopy measurements of single particles in air: A review," Oct. 01, 2021, *IOP Publishing Ltd*. doi: 10.1088/1361-6501/ac0acf.
[62] Z. Gong, Y. Le Pan, G. Videen, and C. Wang, "Optical trapping and manipulation of single particles in air: Principles, technical details, and applications," Jul. 01, 2018, *Elsevier Ltd*. doi: 10.1016/j.jqsrt.2018.04.027.

[63] S. C. Takatori, R. De Dier, J. Vermant, and J. F. Brady, “Acoustic trapping of active matter,” *Nat. Commun.*, vol. 7, Mar. 2016, doi: 10.1038/ncomms10694.
[64] F. T. Gucker and J. J. Egan, “Measurement of the angular variation of light scattered from single aerosol droplets,” *J. Colloid Sci.*, vol. 16, no. 1, pp. 68–84, Feb. 1961, doi: 10.1016/0095-8522(61)90064-2.
[65] P. J. Wyatt and D. T. Phillips, “A new instrument for the study of individual aerosol particles,” *J. Colloid Interface Sci.*, vol. 39, no. 1, pp. 125–135, Apr. 1972, doi: 10.1016/0021-9797(72)90150-6.
[66] E. J. Davis and E. Chorbajian, “The Measurement of Evaporation Rates of Submicron Aerosol Droplets,” *Ind. Eng. Chem. Fundam.*, vol. 13, no. 3, pp. 272–277, Aug. 1974, doi: 10.1021/i160051a021.
[67] A. K. Ray, A. Souyri, E. J. Davis, and T. M. Allen, “Precision of light scattering techniques for measuring optical parameters of microspheres,” *Appl. Opt.*, vol. 30, no. 27, 1991, doi: 10.1364/AO.30.003974.
[68] V. A. Romanov and A. M. Yurkin, “Single-Particle Characterization by Elastic Light Scattering,” *Laser Photonic Rev.*, 2021, doi: 10.1002/lpor.202000368.
[69] T. Serre *et al.*, “A Theory of Object Recognition: Computations and Circuits in the Feedforward Path of the Ventral Stream in Primate Visual Cortex,” Cambridge, 2005. [Online]. Available: http://hdl.handle.net/1721.1/36407
[70] Christopher M. Bishop, *Pattern Recognition and Machine Learning*. Springer, 2006.
[71] A. Ishimaru, S. Kitamura, R. J. Marks, L. Tsang, C. M. Lam, and D. C. Park, “Particle-size distribution determination using optical sensing and neural networks,” *Opt. Lett.*, vol. 15, no. 21, p. 1221, Nov. 1990, doi: 10.1364/OL.15.001221.
[72] P. Qashqai, K. Al-Haddad, and R. Zgheib, “Modeling Power Electronic Converters Using A Method Based on Long-Short Term Memory (LSTM) Networks,” in *IECON Proceedings (Industrial Electronics Conference)*, IEEE Computer Society, Oct. 2020, pp. 4697–4702. doi: 10.1109/IECON43393.2020.9255375.
[73] M. Maruyama, F. Girosi, and T. Poggio, “A Connection between GRBF and MLP,” 1992, [Online]. Available: http://hdl.handle.net/1721.1/6566
[74] F. Rosenblatt, “The perceptron: A probabilistic model for information storage and organization in the brain,” *Psychol. Rev.*, vol. 65, no. 6, pp. 386–408, 1958, doi: 10.1037/h0042519.
[75] V. Nair and G. E. Hinton, “Rectified Linear Units Improve Restricted Boltzmann Machines,” in *Proceedings of the 27th International Conference on Machine Learning*, Haifa, Israel, 2010. [Online]. Available: www.cs.toronto.edu/reluICML
[76] A. Ishimaru, R. J. Marks, L. Tsang, C. M. Lam, D. C. Park, and S. Kitamura, “Particle-size distribution determination using optical sensing and neural networks,” 1990.
[77] Z. Ulanowski, Z. Wang, P. H. Kaye, and I. K. Ludlow, “Application of neural networks to the inverse light scattering problem for spheres,” *Appl. Opt.*, vol. 37, no. 18, p. 4027, 1998, doi: 10.1364/ao.37.004027.
[78] V. V Berdnik and V. A. Loiko, “Retrieval of size and refractive index of spherical particles by multiangle light scattering: neural network method application,” *Appl. Opt.*, vol. 48, no. 32, p. 6178, Nov. 2009, doi: 10.1364/AO.48.006178.
[79] P. Kaye, E. Hirst, and Z. Wang-Thomas, “Neural-network-based spatial light-scattering instrument for hazardous airborne fiber detection,” *Appl. Opt.*, vol. 36, no. 24, p. 6149, Aug. 1997, doi: 10.1364/AO.36.006149.
[80] T. Jakubczyk, D. Jakubczyk, and A. Stachurski, “Assessing the properties of a colloidal suspension with the aid of deep learning,” *J. Quant. Spectrosc. Radiat. Transf.*, vol. 261, no. Ml, p. 107496, Mar. 2021, doi: 10.1016/j.jqsrt.2020.107496.
[81] K. Nyandey and D. Jakubczyk, “Combining transmission speckle photography and

convolutional neural network for determination of fat content in cow milk: an exercise in classification of parameters of a complex suspension," *Eur. Phys. J. Plus*, vol. 139, no. 2, p. 123, Feb. 2024, doi: 10.1140/epjp/s13360-024-04900-1.
[82] D. Gagnon and L. J. Dubé, "Lorenz-Mie theory for 2D scattering and resonance calculations," Sep. 22, 2015, *IOP Publishing Ltd*. doi: 10.1088/2040-8978/17/10/103501.
[83] J. J. Wang, G. Gouesbet, Y. P. Han, and G. Gréhan, "Study of scattering from a sphere with an eccentrically located spherical inclusion by generalized Lorenz–Mie theory: internal and external field distribution," *J. Opt. Soc. Am. A*, vol. 28, no. 1, p. 24, Jan. 2011, doi: 10.1364/JOSAA.28.000024.
[84] C. M. Sorensen, "Light Scattering by Fractal Aggregates: A Review," *Aerosol Sci. Technol.*, vol. 35, no. 2, pp. 648–687, Jan. 2001, doi: 10.1080/02786820117868.
[85] M. Quinten and U. Kreibig, "Absorption and elastic scattering of light by particle aggregates," *Appl. Opt.*, vol. 32, no. 30, 1993, doi: 10.1364/AO.32.006173.
[86] M. Kolwas, D. Jakubczyk, J. Archer, and T. Do Duc, "Evolution of mass, surface layer composition and light scattering of evaporating, single microdropletes of SDS/DEG suspension. Shrinking droplet surface as the micelles generator," *J. Quant. Spectrosc. Radiat. Transf.*, vol. 258, p. 107396, Jan. 2021, doi: 10.1016/j.jqsrt.2020.107396.
[87] J. Archer, M. Kolwas, D. Jakubczyk, G. Derkachov, M. Woźniak, and K. Kolwas, "Evolution of radius and light scattering properties of single drying microdroplets of colloidal suspension," *J. Quant. Spectrosc. Radiat. Transf.*, vol. 202, pp. 168–175, Nov. 2017, doi: 10.1016/j.jqsrt.2017.08.004.
[88] M. Woźniak *et al.*, "Formation of Highly Ordered Spherical Aggregates from Drying Microdroplets of Colloidal Suspension," *Langmuir*, vol. 31, no. 28, pp. 7860–7868, Jul. 2015, doi: 10.1021/acs.langmuir.5b01621.
[89] Y. Shopa *et al.*, "Luminescent nanoparticles in a shrinking spherical cavity – probing the evaporating microdroplets of colloidal suspension – optical lattices and structural transitions," Feb. 01, 2023, *Elsevier Ltd*. doi: 10.1016/j.jqsrt.2022.108439.
[90] C. Oh and C. M. Sorensen, "Scaling Approach for the Structure Factor of a Generalized System of Scatterers," *J. Nanoparticle Res.*, vol. 1, no. 3, pp. 369–377, Sep. 1999, doi: 10.1023/A:1010033111039.
[91] Y. LeCun *et al.*, "Backpropagation applied to handwritten zip code recognition," *Neural Comput.*, vol. 1, no. 4, pp. 541–551, 1989, doi: 10.1162/neco.1989.1.4.541.
[92] Y. Lecun, E. Bottou, Y. Bengio, and P. Haffner, "Gradient-Based Learning Applied to Document Recognition," *Proc. IEEE*, vol. 86, no. 11, pp. 2278–2324, 1998, doi: 10.1109/5.726791.
[93] L. Yann and B. Yoshua, "Convolutional Networks for Images, Speech, and Time-Series," *Handb. brain theory neural networks*, pp. 255–258, 1995, [Online]. Available: https://www.researchgate.net/profile/Yann_Lecun/publication/2453996_Convolutional_Networks_for_Images_Speech_and_Time-Series/links/0deec519dfa2325502000000.pdf%0Ahttps://www.researchgate.net/profile/Yann_Lecun/publication/2453996_Convolutional_Networks_fo
[94] A. Krizhevsky, I. Sutskever, and G. E. Hinton, "ImageNet classification with deep convolutional neural networks," *Commun. ACM*, vol. 60, no. 6, pp. 84–90, May 2017, doi: 10.1145/3065386.
[95] P. Y. Simard, D. Steinkraus, and J. C. Platt, "Best practices for convolutional neural networks applied to visual document analysis," *Proc. Int. Conf. Doc. Anal. Recognition, ICDAR*, vol. 2003-Janua, no. September 2003, pp. 958–963, 2003, doi: 10.1109/ICDAR.2003.1227801.
[96] J. Friedman, T. Hastie, and R. Tibshirani, *The Elements of Statistical Learning: Data*

Mining, Inference and Prediction. 2008. doi: 10.1016/B978-0-12-823939-1.05001-1.
[97] M. Woźniak, D. Jakubczyk, G. Derkachov, and J. Archer, "Sizing of single evaporating droplet with Near-Forward Elastic Scattering Spectroscopy," *J. Quant. Spectrosc. Radiat. Transf.*, vol. 202, pp. 335–341, Nov. 2017, doi: 10.1016/j.jqsrt.2017.08.017.
[98] P. L. Marston and E. H. Trinh, "Hyperbolic umbilic diffraction catastrophe and rainbow scattering from spheroidal drops," *Nature*, vol. 312, no. 5994, pp. 529–531, Dec. 1984, doi: 10.1038/312529a0.
[99] B. Steiner, B. Berge, R. Gausmann, J. Rohmann, and E. Rühl, "Fast in situ sizing technique for single levitated liquid aerosols," *Appl. Opt.*, vol. 38, no. 9, p. 1523, Mar. 1999, doi: 10.1364/AO.38.001523.
[100] E. J. Davis and R. Periasamy, "Light-Scattering and Aerodynamic Size Measurements for Homogeneous and Inhomogeneous Microspherest," *Langmuir*, vol. 1, no. 3, pp. 373–379, 1985, doi: 10.1021/la00063a020.
[101] R. E. March, "An introduction to quadrupole ion trap mass spectrometry," 1997. doi: 10.1002/(SICI)1096-9888(199704)32:4<351::AID-JMS512>3.0.CO;2-Y.
[102] W. Paul and H. Steinwedel, "Notizen: Ein neues Massenspektrometer ohne Magnetfeld," *Zeitschrift für Naturforsch. A*, vol. 8, no. 7, pp. 448–450, Jul. 1953, doi: 10.1515/zna-1953-0710.
[103] Gennadiy Derkachov, "Badanie rozpraszania światła na mikrokroplach wody zawierających inkluzje.," 2007. [Online]. Available: https://www.ifpan.edu.pl/nauka/rozprawy-doktorskie/2008/mgr-gennadiy-derkachov.html?highlight=WyJnZW5uYWRpeSIsImdlbm5hZGl5YSJd
[104] I. Szabo, "New ion-optical devices utilizing oscillatory electric fields. I. Principle of operation and analytical theory of multipole devices with two-dimensional electric fields," *Int. J. Mass Spectrom. Ion Process.*, vol. 73, no. 3, pp. 197–235, 1986, doi: 10.1016/0168-1176(86)80001-5.
[105] J. Archer, "PhD Thesis: Investigation of surfaces of evaporating microdroplets of colloidal suspensions," 2017. [Online]. Available: https://www.ifpan.edu.pl/nauka/rozprawy-doktorskie/2018/mgr-justice-archer.html?highlight=WyJqdXN0aWNlIl0=
[106] H. L. Partner, J. Zoll, A. Kuhlicke, and O. Benson, "Printed-circuit-board linear Paul trap for manipulating single nano- and microparticles," *Rev. Sci. Instrum.*, vol. 89, no. 8, Aug. 2018, doi: 10.1063/1.5007924.
[107] M. I. Jacobs, J. F. Davies, L. Lee, R. D. Davis, F. Houle, and K. R. Wilson, "Exploring Chemistry in Microcompartments Using Guided Droplet Collisions in a Branched Quadrupole Trap Coupled to a Single Droplet, Paper Spray Mass Spectrometer," *Anal. Chem.*, vol. 89, no. 22, pp. 12511–12519, Nov. 2017, doi: 10.1021/acs.analchem.7b03704.
[108] G. Sageev, J. H. Seinfeld, and R. C. Flagan, "Particle sizing in the electrodynamic balance," *Rev. Sci. Instrum.*, vol. 57, no. 5, pp. 933–936, 1986, doi: 10.1063/1.1138837.
[109] E. Bar-Ziv and A. F. Sarofim, "The electrodynamic chamber: A tool for studying high temperature kinetics involving liquid and solid particles," *Prog. Energy Combust. Sci.*, vol. 17, no. 1, pp. 1–65, Jan. 1991, doi: 10.1016/0360-1285(91)90002-5.
[110] E. E. Allison and B. R. F. Kendall, "Cubic electrodynamic levitation trap with transparent electrodes," *Rev. Sci. Instrum.*, vol. 67, no. 11, pp. 3806–3812, 1996, doi: 10.1063/1.1147281.
[111] S. Arnold, "A three-axis spherical void electrodynamic levitator trap for microparticle experiments," *Rev. Sci. Instrum.*, vol. 62, no. 12, pp. 3025–3028, 1991, doi:

10.1063/1.1142149.
[112] C. A. Ward and G. Fang, “Expression for predicting liquid evaporation flux: Statistical rate theory approach,” *Phys. Rev. E*, vol. 59, no. 1, pp. 429–440, Jan. 1999, doi: 10.1103/PhysRevE.59.429.
[113] F. M. Penning, “Die glimmentladung bei niedrigem druck zwischen koaxialen zylindern in einem axialen magnetfeld,” *Physica*, vol. 3, no. 9, pp. 873–894, Nov. 1936, doi: 10.1016/s0031-8914(36)80313-9.
[114] R. S. Van Dyck, P. B. Schwinberg, and H. G. Dehmelt, “Precise measurements of axial, magnetron, cyclotron, and spin-cyclotron-beat frequencies on an isolated 1-meV electron,” *Phys. Rev. Lett.*, vol. 38, no. 7, pp. 310–314, 1977, doi: 10.1103/PhysRevLett.38.310.
[115] D. Jakubczyk, G. Derkachov, M. Kolwas, and K. Kolwas, “Combining weighting and scatterometry: Application to a levitated droplet of suspension,” *J. Quant. Spectrosc. Radiat. Transf.*, vol. 126, pp. 99–104, Sep. 2013, doi: 10.1016/j.jqsrt.2012.11.010.
[116] D. Jakubczyk, S. Migacz, G. Derkachov, M. Woźniak, J. Archer, and K. Kolwas, “Optical diagnostics of a single evaporating droplet using fast parallel computing on graphics processing units,” *Opto-Electron. Rev*, vol. 24, no. 3, 2016, doi: 10.1515/oere−2016−0019.
[117] M. Kolwas, D. Jakubczyk, T. Do Duc, and J. Archer, “Evaporation of a free microdroplet of a binary mixture of liquids with different volatilities,” *Soft Matter*, vol. 15, no. 8, pp. 1825–1832, 2019, doi: 10.1039/C8SM02220H.
[118] R. Hołyst *et al.*, “Evaporation of freely suspended single droplets: Experimental, theoretical and computational simulations,” *Reports Prog. Phys.*, vol. 76, no. 3, Mar. 2013, doi: 10.1088/0034-4885/76/3/034601.
[119] G. Derkachov, D. Jakubczyk, M. Woźniak, J. Archer, and M. Kolwas, “High-precision temperature determination of evaporating light-absorbing and non-light-absorbing droplets,” *J. Phys. Chem. B*, vol. 118, no. 43, pp. 12566–12574, Oct. 2014, doi: 10.1021/jp508823z.
[120] Y. Zhang, G. Hu, Y. Liu, J. Wang, G. Yang, and D. Li, “Suppression and Utilization of Satellite Droplets for Inkjet Printing: A Review,” *Processes*, vol. 10, no. 5, p. 932, May 2022, doi: 10.3390/pr10050932.
[121] A. U. Chen and O. A. Basaran, “A new method for significantly reducing drop radius without reducing nozzle radius in drop-on-demand drop production,” *Phys. Fluids*, vol. 14, no. 1, 2002, doi: 10.1063/1.1427441.
[122] D. Jakubczyk, G. Derkachov, K. Nyandey, S. Alikhanzadeh-Arani, and A. Derkachova, “Chromatic dispersion and thermal coefficients of hygroscopic liquids: 5 glycols and glycerol,” *Sci. Data*, vol. 10, no. 1, Dec. 2023, doi: 10.1038/s41597-023-02819-3.
[123] D. Jakubczyk, G. Derkachov, K. Nyandey, S. Alikhanzadeh-Arani, and A. Derkachova, “Author Correction: Chromatic dispersion and thermal coefficients of hygroscopic liquids: 5 glycols and glycerol,” Dec. 01, 2024, *Nature Research*. doi: 10.1038/s41597-024-03547-y.
[124] S. A. Self, “Focusing of spherical Gaussian beams,” *Appl. Opt.*, vol. 22, no. 5, 1983, doi: 10.1364/AO.22.000658.
[125] H. C. Van De Hulst and R. T. Wang, “Glare points,” *Appl. Opt.*, vol. 30, no. 33, 1991, doi: 10.1364/AO.30.004755.
[126] S. Dehaeck and J. P. A. J. Van Beeck, “Multifrequency interferometric particle imaging for gas bubble sizing,” *Exp. Fluids*, vol. 45, no. 5, pp. 823–831, Nov. 2008, doi: 10.1007/s00348-008-0502-8.
[127] M. Maeda, T. Kawaguchi, and K. Hishida, “Novel interferometric measurement of size

and velocity distributions of spherical particles in fluid flows," *Meas. Sci. Technol.*, vol. 11, no. 12, 2000, doi: 10.1088/0957-0233/11/12/101.
[128] M. Guillon and B. Stout, "Optical trapping and binding in air: Imaging and spectroscopic analysis," *Phys. Rev. A - At. Mol. Opt. Phys.*, vol. 77, no. 2, Feb. 2008, doi: 10.1103/PhysRevA.77.023806.
[129] Y. Wu, H. Li, M. Brunel, J. Chen, G. Gréhan, and L. Mädler, "Phase interferometric particle imaging for simultaneous measurements of evaporating micron-sized droplet and nanoscale size changes," *Appl. Phys. Lett.*, vol. 111, no. 4, 2017, doi: 10.1063/1.4996363.
[130] S. Rydblom and B. Thörnberg, "Liquid water content and droplet sizing shadowgraph measuring system for wind turbine icing detection," *IEEE Sens. J.*, vol. 16, no. 8, pp. 2714–2725, Apr. 2016, doi: 10.1109/JSEN.2016.2518653.
[131] "Journal policies | Open science | Springer Nature." Accessed: Jun. 02, 2025. [Online]. Available: https://www.springernature.com/gp/open-science/policies/journal-policies
[132] K. Nyandey, "Sample laser speckle images generated from commercial milk in thin cuvette," vol. 1, 2023, doi: 10.17632/PG9Z22D9PZ.1.
[133] "Copyright | Elsevier policy." Accessed: May 30, 2025. [Online]. Available: https://www.elsevier.com/about/policies-and-standards/copyright
[134] K. Nyandey, G. Derkachov, and D. Jakubczyk, "A convolutional neural network technique for online tracking of the radius evolution of levitating evaporating microdroplets of pure liquids, liquid mixtures and suspensions," *J. Quant. Spectrosc. Radiat. Transf.*, vol. 344, no. October 2024, p. 109533, May 2025, doi: 10.1016/j.jqsrt.2025.109533.
[135] K. Nyandey, "A convolutional neural network technique for online tracking of the radius evolution of levitating evaporating microdroplets of pure liquids, liquid mixtures and suspensions - Mendeley Data." Accessed: May 30, 2025. [Online]. Available: https://data.mendeley.com/datasets/4fhwb3kjkn/2

Dostępy do artykułów:

K. Nyandey and D. Jakubczyk, “Combining transmission speckle photography and convolutional neural network for determination of fat content in cow milk: an exercise in classification of parameters of a complex suspension,” Eur. Phys. J. Plus, vol. 139, no. 2, Feb. 2024, https://doi.org/10.1140/epjp/s13360-024-04900-1.

K. Nyandey, G. Derkachov, and D. Jakubczyk, “A convolutional neural network technique for online tracking of the radius evolution of levitating evaporating microdroplets of pure liquids, liquid mixtures and suspensions,” *J. Quant. Spectrosc. Radiat. Transf.*, vol. 344, no. 2024, p. 109533, May 2025, https://doi.org/10.1016/j.jqsrt.2025.109533